J. Fluid Mech. (1982), *vol.* 125, *pp.* 219–258
Printed in Great Britain

Heat transport and temporal evolution of fluid flow near the Rayleigh–Bénard instability in cylindrical containers

By R. P. BEHRINGER
Department of Physics, Duke University, Durham, NC 27706

AND GUENTER AHLERS
Department of Physics, University of California, Santa Barbara, CA 93106

(Received 7 October 1981 and in revised form 13 May 1982)

First this paper describes in detail an apparatus for heat-transport measurements in shallow horizontal layers of fluid at low temperatures. Then high-precision results of convective heat transport as a function of the Rayleigh number R are presented for cylindrical cells of aspect ratio $L = 2{\cdot}08$, $4{\cdot}72$ and 57. The present paper concentrates on the long-time behaviour of Boussinesq systems. Non-Boussinesq effects, transient effects near the convective onset, and time-dependent states are described elsewhere (Walden & Ahlers 1981; Ahlers *et al.* 1981; Ahlers 1980*b* and references therein). The measurements show that the convective onset near the critical Rayleigh number R_c is sharp within the experimental resolution of about $0{\cdot}1\,\%$ of the Nusselt number N, even in laterally finite containers. Values of R_c, and of the initial slopes of $N(R)$, are obtained and compared with predictions for different flow patterns. Over a wider range of R and for $L = 57$ and $4{\cdot}72$, N was found within experimental resolution to be a unique, continuous function of R. For $L = 2{\cdot}08$, hysteretic transitions are revealed by $N(R)$ near $R \approx 3$ and $R \approx 10$. For $L = 4{\cdot}72$, the effect of impulsive heating was studied and revealed complicated, long-lived, but surprisingly reproducible transients.

CONTENTS

1. Introduction

Measurements of heat transport have long been an important tool for the study of the Rayleigh–Bénard instability (Bénard 1900, 1901; Rayleigh 1916) and the subsequent evolution of time-dependent flow states in a shallow, horizontal layer of fluid heated from below (Schmidt & Milverton 1935; Schmidt & Saunders 1938; Malkus 1954; Silveston 1958; Willis & Deardorff 1967; Krishnamurti 1968, 1970*a*, *b*, 1973; Rossby 1969; Willis, Deardorff & Somerville 1972; Koschmieder & Pallas 1974; Koschmieder 1974). All of these measurements have been conducted near room temperature, and their resolution generally has been no better than 1 % of the Nusselt number.

We describe in this paper our apparatus and experimental techniques for heat-flow measurements at *cryogenic* temperatures, which, depending on the particular circumstances of the experiment, yield a resolution of one part in 10^3 or 10^4 of the Nusselt number. This greatly enhanced resolution makes possible more advanced experiments that make close contact with recent theoretical developments in this field. Several of the experiments conducted with the apparatus already have been reported elsewhere. They include the study of non-Boussinesq systems and of penetrative convection (Walden & Ahlers 1981), of transient effects near the convective onset (Behringer & Ahlers 1977; Ahlers *et al.* 1981) and of time-dependent flow states (Ahlers & Behringer 1978*a*, *b*; Ahlers 1980*b*; Ahlers & Walden 1980; Greenside *et al.* 1982). The experimental section of this paper thus provides the foundation for those previous publications.

In addition, we report here the results of Nusselt-number measurements for cylindrical cells of various aspect ratios and filled with Boussinesq fluids. We have concentrated here on the behaviour of our systems in the long-time limit. But we also report on our observations of very complicated, long-lived, but completely reproducible, transients that occur when the system is heated impulsively into the convecting state.

Prior to the work described in this paper, the Rayleigh–Bénard problem had been studied at low temperatures by Ahlers (1974, 1975, 1980*b*), by Threlfall (1975), by Libchaber & Maurer (1978, 1980, 1981) and by Maurer & Libchaber (1979, 1980). The present apparatus represents a considerable refinement over that used by Ahlers

(1974, 1975, 1980*a*). The low-temperature measurements have several advantages, which we will list briefly.

(i) One can resolve temperature changes of 10^{-7} K, thus yielding a resolution and thermal stability $\delta T/T$ of about 5×10^{-8} when $T \approx 2$ K (Ahlers 1971*a*).

(ii) One can design the apparatus in such a way that any extraneous heat transport parallel to the convecting fluid is very small and readily measured. This is because of the almost complete absence of heat transport by radiation, and because of the great variation in the thermal conductivity of materials at low temperatures. Thus the lateral walls of a convection cell can have thermal conductivities of 10^{-3} to 10^{-5} W cm^{-1} K^{-1}. There is also no heat transport by convection or conduction in fluid outside the cell, since the experiment is suspended in an extremely good, cryo-pumped vacuum.

(iii) The boundary conditions of uniform temperature at the top and bottom plate can be approximated extremely well because the horizontal boundary plates can be made of copper, which has a conductivity of several W cm^{-1} K^{-1} even at $T = 2$ K. For the fluid (liquid or gaseous helium) the thermal conductivity is in the range 5×10^{-5} to 2×10^{-4} W cm^{-1} K^{-1}. The large ratio between these conductivities results in exceedingly small horizontal thermal gradients in the end plates of the cell.

(iv) The high thermal conductivity of copper, together with its very small heat capacity at low temperatures, yields horizontal thermal diffusion times in the end plates ($\approx 10^{-3}$ s if typical lengths are of order 1 cm) that are much smaller than any timescale associated with time-dependent phenomena in the fluid flow. Thus, even for turbulent flow, the top- and bottom-plate temperatures remain uniform in the horizontal plane.

(v) The extremely small heat capacity of copper compared with that of liquid helium makes it possible to measure the time dependence of the convective heat transport by turbulent fluid flow without significant high-frequency damping due to the thermal mass of the container. This can be appreciated readily on the basis of the ratio between the heat capacity per unit volume of typical solids at low temperatures and liquid helium. This ratio is about 10^{-3}. Thus even a cell with top or bottom plates that are ten times as voluminous as the fluid will have only a small damping effect upon the amplitudes of time-dependent processes. A discussion of this damping is given by Behringer *et al.* (1980).

(vi) The properties of cryogenic fluids provide great flexibility. By judicious choice of the operating temperature and pressure for either gaseous or liquid helium, convecting systems can be established which are either well represented by or depart significantly from the Oberbeck–Boussinesq approximation (Oberbeck 1879; Boussinesq 1903; Ahlers 1980*a*; Walden & Ahlers 1981).

(vii) The investigation of convection in mixtures of ^{3}He and ^{4}He, both normal and superfluid, has barely begun (Lee, Lucas & Tyler 1979; Warkentin, Haucke & Wheatley 1980) and potentially is a very rich field for the study of a great variety of phenomena (Steinberg 1980, 1981*a*, *b* and private communication).

Finally, one must recognize also the limitations and disadvantages of the low-temperature convection studies. Perhaps the most serious limitation is that one can only study fluids with Prandtl numbers near unity unless one works in the obviously difficult range near the phase transitions. The reason for this is that the transport properties of these fluids are well approximated by those of a hard-sphere gas, and such a gas has a Prandtl number equal to $\frac{2}{3}$ (Hirschfelder, Curtiss & Bird 1967). The second disadvantage is that flow visualization is difficult to accomplish, and optical access to the fluid is not easily obtained. For these reasons, most low-temperature

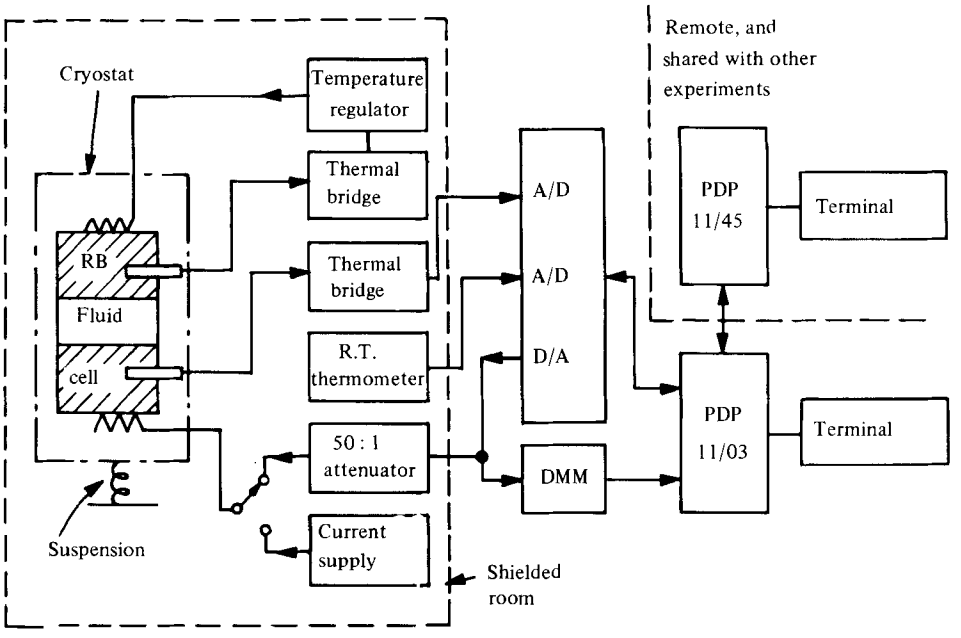

FIGURE 1. Schematic representation of the experimental apparatus.

measurements have been global measurements of the total heat flux. Local measurements of the flow are possible, however, and have been made by Ahlers & Behringer (1978*a*), Libchaber & Maurer (1978, 1980, 1981) and Maurer & Libchaber (1979, 1980).

In §2 we describe the cryogenic apparatus and the convection cells in detail. Section 3 contains definitions of the symbols used in the remainder of the paper, and preliminary measurements of properties of the empty convection cells are discussed in §4. The procedure used in heat-flow measurements is illustrated in §5. In §6, the fluid properties and the calculation of Rayleigh numbers are discussed. Our results are presented in §7. They fall into several categories. Section 7.1 presents the experimental critical Rayleigh numbers for two different aspect ratios. In §7.2, we discuss the rounding near the convective onset, which is always present owing to the imperfect bifurcation in real experimental cells. Section 7.3 contains the results for Nusselt-number measurements near R_c. Comparison with theory of values of R_c and of the initial slope of $N(R)$ near R_c yields considerable information about the symmetry of the flow. Nusselt numbers at larger R are presented in §7.4. The uniqueness of $N(R)$ is discussed in §7.5, and §7.6 presents the results on transient effects due to impulsive heating.

2. Apparatus

2.1. *General arrangement*

The experiments described below and elsewhere (Behringer & Ahlers 1977; Ahlers & Behringer 1978*a*, *b*; Ahlers 1980*b*; Ahlers & Walden 1980; Walden & Ahlers 1981; Ahlers *et al.* 1981; Greenside *et al.* 1982) required a system that for periods of up to a week permitted continuous automated data taking in the absence of excessive mechanical and electromagnetic interference. A schematic diagram of the system used by us is given in figure 1.

A commercially available copper double-walled singly connected shielded room contained all parts of the experiment that involved low-level signals and thus

provided protection against electrical disturbances. High-level signals could be brought into and out of this room by means of coaxial feedthroughs for the purpose of interfacing to a digital minicomputer. The computer was deliberately left outside the shielded room to avoid possible interference from the high-frequency switching of high-level signals that take place in it.

Mechanical vibration isolation was provided for the experiment by placing the entire cryostat on a bellows-sealed gas suspension system inside the shielded room. The effectiveness of this system was determined by measuring the temperature drop at the bottom of a Rayleigh–Bénard (RB) cell ($\approx 2\,\mu$K for cell A) due to raising the cryostat on the suspension system. Typically, the reduction in heat input to the bottom of the cell corresponding to this temperature drop was 8 nW, or 0·4 % of the critical power for the RB instability in cell A. We expect that any residual mechanical-energy input to the bottoms of the RB cells was an order of magnitude below this level. In addition, the vibration isolation system reduces to an extremely low level the amplitudes of any mechanical modes that might couple to the fluid flow.

In order to obtain up to 6 days of data-taking time without interruption for the transfer of helium, a Dewar flask with a liquid capacity of about 25 l was used. An automatic data-acquisition system (Wonsiewicz, Storm & Sieber 1978) provided the uninterrupted data-taking capability required especially for characterizing time-dependent flow states (Ahlers & Walden 1980; Ahlers & Behringer 1978*a*, *b*; Greenside *et al.* 1982).

2.2. *Cryogenic apparatus*

2.2.1. *General arrangement.* Figure 2 depicts the low-temperature portion of the apparatus, which was contained within a vacuum can immersed in liquid ^{4}He at 4·2 K. All tubes entering this portion of the apparatus were baffled against radiation leaks. Below the top of the vacuum can was a continuously operating self-regulated ^{4}He evaporator (DeLong, Symko & Wheatley 1971) having a volume of 2 cm^3 and capable of maintaining, to within a few mK, a temperature near 1·3 K. Proceeding downwards, the next stage was a continuously operating ^{3}He evaporator comparable in size to the ^{4}He refrigerator.

Between the ^{3}He refrigerator and the sample chamber was a temperature-regulated buffer stage or isothermal platform (Ahlers 1971*a*). By filtering out most of the thermal fluctuations in the cooling stages, the isothermal platform provided a stable environment for performing high-precision thermal measurements.

2.2.2. *Helium reservoir.* A reservoir made of OFHC copper was suspended from the isothermal platform by three 0·95 cm diameter × 12 cm long nylon rods. The large heat capacity of the helium-filled reservoir served as a sink to help absorb variations in the heat applied to the Rayleigh–Bénard cells. The reservoir was made in three sections, the middle one containing almost all of the helium and consisting of a series of grooves of height 0·51 cm and width 0·08 cm, separated by 0·08 cm of copper. The volume available to the helium was 17·6 cm^3. All of the liquid was within 0·04 cm of a copper surface, guaranteeing thermal relaxation times in the reservoir of no more than a few seconds. Soldered into the top section was a beryllium–copper strain gauge, which served as a pressure transducer (Straty & Adams 1969). Three different Rayleigh–Bénard cells were screwed to the bottom section, which was supplied with an indium-gasket-sealed capillary connector for each of the three cells. The sections of the reservoir were sealed together with indium gaskets, and different experiments can be performed with the same apparatus by replacing one or more of the sections.

The reservoir was filled through a low-temperature valve (Mueller, Ahlers & Pobell 1976), and all the helium below the valve seat was linked thermally to the reservoir by a thick copper braid.

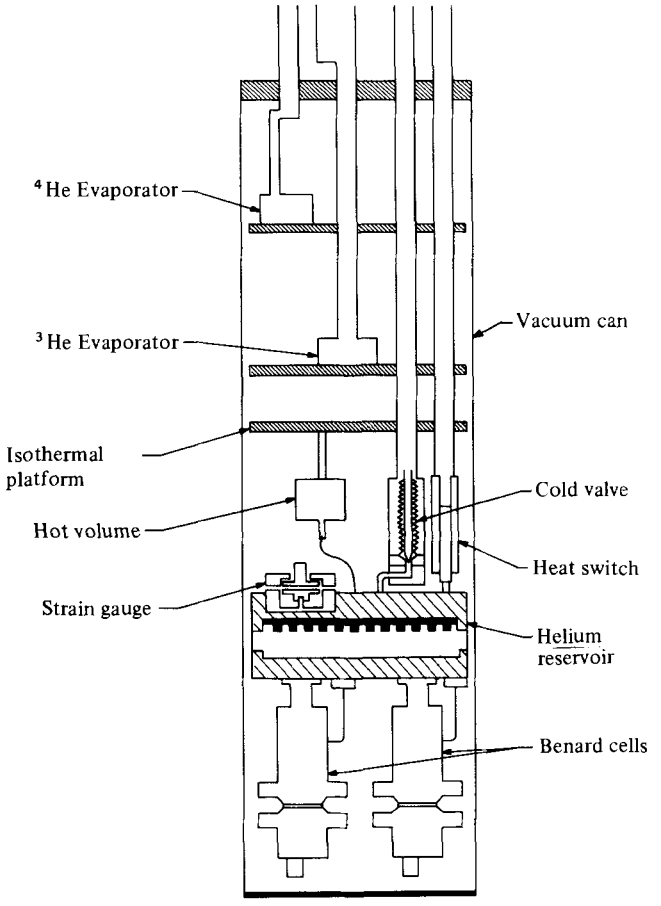

FIGURE 2. Schematic representation (to scale) of the cryostat. The diameter of the vacuum can is 5·75 in.

2.2.3. *Pressure measurement and regulation.* A three-lead bridge technique was used to measure the capacitance of the strain gauge. Two arms of the bridge were contained in a commercial bridge,† one arm was the strain gauge (capacitance = C_g) and the remaining arm was a low-temperature standard capacitor (capacitance = C_s) mounted on the helium reservoir. We could resolve pressure changes of 10^{-6} bar over a range of 0–30 bar. The zero-pressure change in C_g/C_s over the temperature range 1·3–5·4 K amounted to twenty times the gauge resolution, but for practical purposes was ignorable.

The strain gauge was calibrated against a Texas Instruments bourdon gauge,‡ which had in turn been calibrated against a dead-weight tester. The accuracy of the strain-gauge pressures is $\pm 5 \times 10^{-4}$ bar.

When liquid and vapour phases were both present in the reservoir, the pressure was controlled by regulating the temperature. When only one phase was present, the pressure was separately controlled by a 'hot-volume' technique, as described by Mueller *et al.* (1976).

2.2.4. *Temperature measurement and regulation.* On each of the ^{3}He refrigerator, the

† General Radio, Co., Concord, Mass, Type 1615A Capacitance Bridge.
‡ Texas Instruments, Inc., Houston, Texas, Model 145.

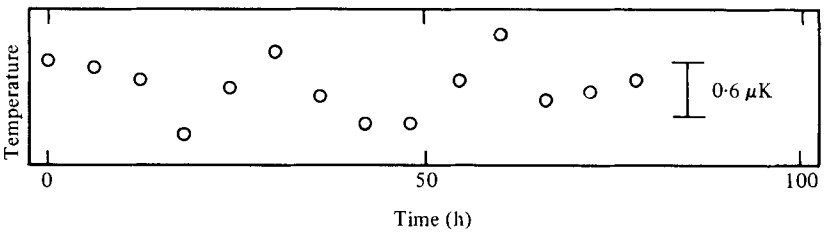

FIGURE 3. Long-term thermal stability of a Rayleigh–Bénard cell when mounted in the cryostat shown in figure 2 (cell A).

isothermal platform, the hot volume and the reservoir there was mounted one germanium thermometer,† while each of the Rayleigh–Bénard cells required two germanium thermometers, one on either end. Each thermometer was mounted in a snug-fitting hole in an OFHC copper post. The leads were heat sunk to the post, and around each post were wound two non-inductive reference resistors. By wrapping the reference resistors on the thermometer mount, the very small temperature dependence of its resistance was automatically incorporated in the calibration of the germanium thermometer. A germanium thermometer was paired with one of its reference resistors and incorporated in a five-lead bridge (Mueller *et al.* 1976). The temperature resolution of such a bridge depends, of course, on the averaging time, but in much of the work to be reported here was about 1×10^{-7} K. There were no measurable long-term (over, say, a week) drifts, but variations by typically 4×10^{-7} K occurred with periods of approximately a day. This is illustrated in figure 3. Shown there are the temperatures at the bottom of cell A, measured once every six hours, while the thermometer at the top of the cell was used to regulate the temperature. For comparison, 0·1 % of the temperature difference corresponding to the critical Rayleigh number is 0·6 μK and is shown in the figure.

The thermometers were calibrated against the ^{4}He vapour pressure scale (van Dijk *et al.* 1960) (T^{58}). Deviations of our scale from T^{58} are no more than $\pm 0{\cdot}2$ mK.

Temperature regulation was provided by using the appropriate thermometer bridge out of balance to activate a temperature controller‡ driving a heater.

2.2.5. *Heat leaks.* During these measurements the ^{3}He refrigerator was not used, and a thermal buss consisting of a thick copper braid was used to link the ^{3}He refrigerator thermally to the ^{4}He refrigerator. For rapid cooling of the sample, there was a mechanical heat switch between the ^{3}He refrigerator and the helium reservoir. Heat leaks of 8×10^{-4} W K^{-1} between the reservoir and the isothermal platform and 7×10^{-3} W K^{-1} between the isothermal platform and the ^{3}He stage permitted maximum power inputs to the cells of $0{\cdot}65 \times 10^{-3}$ W and $2{\cdot}8 \times 10^{-3}$ W at 2·2 K and 5·4 K respectively.

2.3. *Rayleigh–Bénard cells*

2.3.1. *Design and construction.* Three different Bénard cells were suspended simultaneously from the sample chamber. In these experiments the cells were specifically designed for high-precision Nusselt-number measurements. Each cell was cylindrical, and considerable care was taken to ensure that the departures from ideal geometry were minimized without jeopardizing the quality of the cell as an instrument for measuring heat transport. Figure 4 shows a cross-section of the cells, and table 1 gives the diameter D, height d and aspect ratio $L = D/2d$ of the cells. For two of them

† Cryocal Inc., 5301 Industrial Blvd, Edina, Minn.

‡ Linear Research, P.O. Box 9308, San Diego, CA., Mod. LR-130.

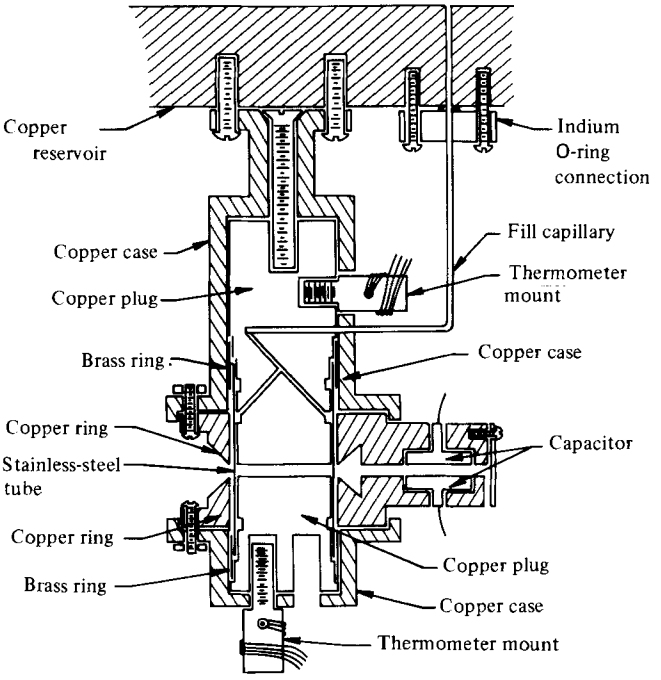

FIGURE 4. Schematic representation (to scale) of a Rayleigh–Bénard cell.

Cell	A	B	C	D
D (cm)	2·502	1·076	2·502	0·926
d (cm)	0·265	0·259	0·022	0·088
δd (μm)	7·6 ± 7·6	15·0 ± 10·0	15·0 ± 10·0	—
L	4·72	2·08	57	5·27

TABLE 1. Cell dimensions

we chose $d \approx 0{\cdot}26$ cm. A larger value would result in excessively large thermal diffusion times, whereas appreciably smaller values of d would result in larger values of $\delta d/d$, where δd is the non-uniformity of d. For cell C we reduced d considerably in order to obtain a large L, and we expect $\delta d/d$ to be relatively large in this case.

Each cell was made by gluing two cylindrical OFHC copper cylinders into a snugly fitting stainless steel tube of wall thickness 0·015 cm using Emerson & Cummings no. 1266 epoxy resin. The walls were sufficiently thin that the majority of the heat transport (88 % for cells A and C and 76 % for cell B) was through the fluid (see §5.2).

The gap between the copper cylinders and the stainless-steel tube was no more than 0·001 cm. In order to prevent epoxy from flowing into the working part of the cell, a ring was cut into each copper cylinder. In order to obtain extra shear strength, brass rings of wall thickness 0·015 cm were glued with epoxy to the outside of the stainless-steel tube and also to the cylinders.

Snug fitting rings made of OFHC copper encircled the stainless-steel tube. Each ring and cylinder were screwed to an outer OFHC copper case, and when assembled each cylinder extended approximately 0·005 cm beyond the corresponding ring. Apiezon N grease was used between the rings and the stainless-steel tube to help improve thermal contact. These rings served two purposes. First, they prevented the

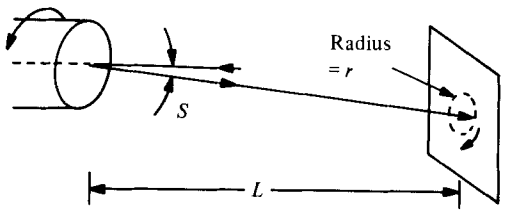

FIGURE 5. Illustration of the method used to determine the parallelity of the cell faces. See text for details.

thin stainless-steel tube from bulging away from the inner copper pieces, thus inhibiting distortion of the cell, and, secondly, they guaranteed that the walls were always in good thermal contact with the horizontal boundaries at their junction. In order to measure the change in cell height with pressure there was suspended rigidly from each ring one plate of a shielded capacitor. The capacitance between the plates was a direct measure of the spacing between the two faces of the cell.

To avoid perturbing the cylindrical geometry, the fill capillaries did not enter the cells in their active portion. Instead, the fluid entered the annulus between the stainless-steel wall and the copper cylinder and then seeped into the main part of the cell.

The thermal mass of the copper in the hot end of the Bénard cells was minimized in order to minimize damping of temperature fluctuations of time-dependent flow states (see Behringer *et al.* 1980). In the worst case the thermal diffusion time between a face of a cell and its thermometer was estimated to be less than 10^{-3} s.

The non-inductive heaters on the hot ends of the cells had a resistance of about 5 kΩ. The heat created by passing a DC current through these resistances was measured by a four-lead potentiometer circuit with an estimated uncertainty in the heater power input to the cells of 0·02 %.

2.3.2. *Cell quality.* The sharpness of the onset of convection depends on the trueness of the cell geometry (Kelly & Pal 1978; Tavantzis, Reiss & Matkowsky 1978; Ahlers 1975; Behringer & Ahlers 1977). We therefore made an effort to obtain a flat, parallel-plate geometry. To obtain uniform, reproducible and unoxidized surfaces, the faces of the cells were lapped to a reflecting finish and coated first with 500 Å of titanium and then 2000 Å of gold by flash evaporation. The flatnesses of the faces were determined with an interferometric technique, and were typically 1 μm. The faces were made as parallel as possible by the following procedure, illustrated in figure 5. For each end of the copper cylinders, the angle ρ between the flat surface and the axis was determined by shining a laser beam at near-normal incidence on the face and then rotating the cylinder in a precision V-block. On rotation, any deviation of ρ from $\frac{1}{2}\pi$ caused the reflected laser spot at a distance L to describe a circle of radius r, and $S \equiv |\frac{1}{2}\pi - \rho| = r/L$. Using these measurements, the cylinders of each cell were assembled so as to make the faces as parallel as possible. After the assembly, the same laser-spot technique was applied again to the outer ends of the cylinders and the relative tilt of the faces was calculated. The corresponding variations δd in the cell height d are given in table 1.

3. Definition of parameters

We use d to denote the height and D the diameter of a cell, and define the dimensionless aspect ratio by

$$L \equiv \frac{D}{2d}.$$

The temperature, in K, at the bottom (hot) end of the cell is T_1 and at the top (cold) end it is T_2. The temperature difference $\Delta T' = T_1 - T_2$ will be normalized by its critical value $\Delta T'_c$ at the onset of convection to yield

$$\Delta T \equiv \frac{\Delta T'}{\Delta T'_c}.$$

The total heat current $Q' = Q'_w + q'$ flowing through a cell consists of the part Q'_w conducted by the walls and the part q' carried by the fluid. The wall conductance l_w is equal to $Q'_w/\Delta T'$. The dimensionless heat flux q carried by the fluid is obtained by normalizing by q'_c (the value of q' when in a steady state $\Delta T = 1$):

$$q \equiv \frac{q'}{q'_c}.$$

The thermal conductivity of the fluid is λ, and is given by $\lambda = 4q'd/D^2\pi\Delta T'$ for $\Delta T' < \Delta T'_c$. The thermal diffusivity and kinematic viscosity are $\kappa = \lambda/\rho C_p$ and $\nu = \eta/\rho$ respectively. Here ρ is the density, C_p the heat capacity at constant pressure per unit mass and η the shear viscosity. We define the Prandtl number as

$$\sigma = \frac{\nu}{\kappa}.$$

The Rayleigh number is taken to be

$$R = \frac{g\beta_p d^3 \Delta T'}{\kappa\nu},$$

where β_p is the isobaric thermal-expansion coefficient, and the Nusselt number is

$$N = \frac{\lambda_{\text{eff}}}{\lambda},$$

where λ_{eff} is the effective thermal conductivity including any heat transport by fluid flow. When the system is in a steady state, we have

$$\frac{(N-1)R}{R_c} = q - \Delta T.$$

The timescale will be set by the vertical thermal diffusion time, and we define

$$t = \frac{t'\kappa}{d^2},$$

where the time t' has units.

4. Preliminary measurements

Before ^{4}He was admitted to the apparatus, the very weak temperature dependences of the strain-gauge capacitance and of the cell-spacing capacitors was determined over the range 1·3 K $\lesssim T \lesssim$ 5 K. We also measured the wall conductance l_w for cells A and B. For cell C, a meaningful measurement of l_w was not possible because of the small value of d. In this case, the effective thermal length of the walls changed appreciably when the cell was filled. We therefore obtained l_w by comparing the measured conductance of the filled cell with the conductance calculated from the thermal conductivity of liquid helium as measured in cell A at several temperatures. Since the thermal conductivity of liquid helium near but above the superfluid transition temperature T_λ decreases rapidly with increasing T, whereas the thermal conductivity

of stainless steel increases, this comparison at several temperatures yielded both the height d and l_w for cell C.

The thermometers on the helium reservoir and on the top sections of the cells were calibrated against the ^{4}He sample vapour pressure, using both an external pressure gauge and the strain gauge on the sample chamber over the ranges from 1·3 to 4·5 K.

Below T_λ, the thermal conductivity of the liquid is effectively infinite, and thus there is no temperature difference between the top and bottom of a cell. Therefore we were able to calibrate the bottom thermometers against the top thermometers with extremely high resolution over the range 1·3–2·17 K. The relative sensitivities of the top and bottom thermometer bridges were within 1 % of each other and could be determined to $\pm 0{\cdot}01$ %. The mild temperature dependence of this sensitivity could easily be extrapolated to 2·184 K, where most of our measurements for cells A and B were made.

Knowing the sensitivity of the bottom thermometers, we were able to determine the temperature change at the cell bottom which was caused by changing the top temperature from just below T_λ to the operating temperature near 2·184 K. Since there are no thermal gradients in the fluid below T_λ, the excess temperature change of the cell bottom was attributable to background heat inputs and the finite thermal conductivity of the fluid above T_λ. The background heating depended upon the power dissipated in the bottom thermometers, but typically yielded a $\Delta T'$ of 40 μK for cell A and 100 μK for cell B when no heater power was dissipated. The thermal conductance of cell C is so large that background-heating effects are negligible.

5. Procedure

5.1. *General procedures*

During all our measurements, the temperature at the top (cold) end of the cell was held fixed by a temperature controller driven by the out-of-balance signal of the cold-end thermometer bridge. For the measurement with the fluid at its vapour pressure (cells A and B), no pressure regulation was needed. Cell C was used in a single-phase region, and, in this case, the pressure was held constant using the hot volume described in §2.2.3.

For cells A and B the cold-end temperature was held fixed at an operating temperature, which was about 12 mK above T_λ at saturated vapour pressure. Since T_λ can be determined on our working temperature scale to better than $0{\cdot}5 \times 10^{-6}$ K, the operating temperature was reproducible to ± 1 μK.

Cell C was operated at points off the saturated vapour pressure curve because its extremely small height $d \approx 0{\cdot}02$ cm required a different set of fluid parameters in order to initiate convection. In this case, the operating temperature was uncertain by a few mK and reproducible to $\pm 0{\cdot}1$ mK.

5.2. *Nusselt-number measurements*

In order to test for possible non-uniqueness of the Rayleigh-number dependence of N, we used two qualitatively different procedures for reaching a steady-state Rayleigh number. In the first, the heat current q was changed discontinuously. Some measurements were made by starting with q near zero and discontinuously changing it to some value greater than unity. On other occasions, q was varied in small, discrete steps. The second method consisted of changing q quasi-continuously by means of a ramp. In that case,

$$q = q_0 + \beta t,$$

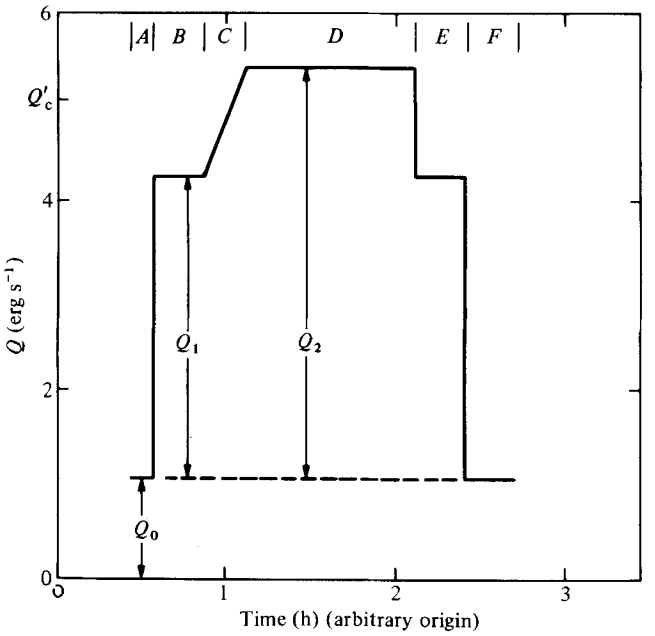

FIGURE 6. Typical sequence of heat currents used in Nusselt-number measurements. The particular example is for cell B.

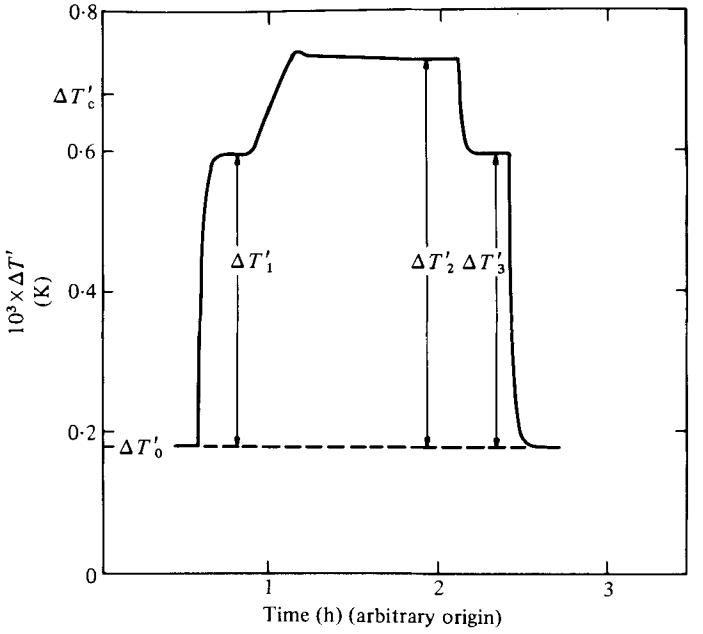

FIGURE 7. Temperature response to the heat current in figure 6 (cell B).

where the dimensionless ramp rate β was usually about equal to 0·01, although larger and smaller rates were used also (Ahlers *et al.* 1981). We will discuss in detail the determination of N using the ramp method.

Figures 6 and 7 represent a typical computer-controlled measurement of N and R, using a ramp in the heat current Q' to enter the convecting state. This example

is for cell B. In figure 6, Q' is shown as a function of time. Here Q'_0 is the background power due primarily to dissipation in the thermometer and radiation from 4·2 K. The remainder of Q' is computer-generated. The temperature response at the bottom of the cell, with the temperature at the top held fixed, is shown in figure 7. There is a $\Delta T'_0$ caused by Q'_0, which was measured as described in §4. The thermal conductance l_0 of the fluid in the absence of convection is determined in segment B (figure 6) of the measurement sequence, and is given by

$$l_0 = \frac{Q'_1}{\Delta T'_1} - l_w$$

where the wall conductance l_w was determined when the cells were empty (see §4). We found that $l_w/(l_0+l_w)$ was equal to 0·12 and 0·24 for cells A and B respectively. For cell C, this ratio should be about the same as for cell A, but we do not have an accurate measurement (see §4). The background power is obtained from $Q'_0 = (l_0+l_w)\Delta T'_0$. During segment C in figures 6 and 7, the ramp is used to pass Q'_c and $\Delta T'_c$. For the case illustrated, the dimensionless ramp rate dq/dt is 0·03, corresponding to $dQ'/dt' = 2{\cdot}3 \times 10^{-9}$ W min^{-1}. The conductance l in the presence of fluid flow is determined in segment D, and is given by

$$l = \frac{Q'_2+Q'_0}{\Delta T'_2+\Delta T'_0} - l_w.$$

Finally, the Nusselt number N is given by l/l_0. This estimate of N neglects of course any lateral heat flow into or out of the fluid because of any difference in the z-dependence of the temperature gradient in the fluid and walls for $R > R_c$.

Sufficiently near R_c, or for a Boussinesq system at any R, we have

$$\frac{R}{R_c} = \frac{\Delta T'_2+\Delta T'_0}{\Delta T'_c} = \Delta T.$$

When there are departures from the Boussinesq approximation, there are corrections to the last equation (see §6.2). Segments E and F provide a check of the temperature measurements in segments A and B.

The above measurement sequence is typical. The sequence of events can of course be changed easily to yield optimum results for a particular situation simply by making software changes.

6. Fluid properties and Rayleigh numbers

6.1. *Fluid properties*

The operating temperatures of cells A and B were $T_2 = 2{\cdot}1841$ K at saturated vapour pressure. In that range, the fluid properties have been studied extensively because they are of interest in relation to continuous phase transitions. The thermodynamic properties can be derived from the measured specific heat (Ahlers 1976), which can be represented by

$$C_p = -A \ln \tilde{t} + B + D\tilde{t} \ln \tilde{t} + E, \tag{6.1}$$

with $A = 5{\cdot}355$, $B = -7{\cdot}77$, $D = 14{\cdot}5$ and $E = 103$ J mol^{-1} K^{-1}. The molar mass is 4·0038 g mol^{-1}, and $\tilde{t} \equiv T/T_\lambda - 1$, where T is the temperature in K and $T_\lambda = 2{\cdot}1720$ K. The above equation is adequate to represent C_p within 1 % for $T_\lambda < T \lesssim 2{\cdot}3$ K. The isobaric thermal-expansion coefficient β_p can be obtained from the measured values

T (K)	η (μP)
2·2	5·4
2·5	6·2
3·0	7·4
3·5	8·9
4·0	10·3
4·5	11·6
5·0	12·9
5·5	14·2
6·0	15·4
7·0	17·6
8·0	19·6
10·0	22·9

TABLE 2. The viscosity of ^{4}He gas at low density

(Van Degrift 1974) of the expansion coefficient at saturated vapour pressure. The fluid density may be regarded constant and equal to 0·1462 g cm^{-3}. The shear viscosity (Ahlers 1971*b*) is well represented by

$$\eta = \eta_\lambda(1 + 1{\cdot}92\tilde{t}^{0{\cdot}811}) \tag{6.2}$$

with $\eta_\lambda = 24{\cdot}9$ μP. Although the dependence upon $\tilde{t}$ is given quite accurately by this equation, the uncertainty in η_λ is perhaps as large as 10 % and is the greatest source of error in Rayleigh-number calculations. The thermal conductivity was measured during the course of this work (Ahlers, Hohenberg & Kornblit 1982), as well as previously (Ahlers 1976) and can be well represented by the empirical equation

$$\lambda = \lambda_0 \tilde{t}^{-0{\cdot}556}(1 + \lambda_1 \tilde{t}^{0{\cdot}636}) \tag{6.3}$$

with $\lambda_0 = 37{\cdot}39$ erg s^{-1} cm^{-1} K^{-1} and $\lambda_1 = 40{\cdot}72$.

Cell C was used near 5·4 K in a single-phase region of density $\rho \approx 0{\cdot}05$ g cm^{-3} where the fluid properties are not known very well. However, we have estimated the Prandtl numbers in the following manner.

We obtained η by interpolating between experimental results at higher and lower densities. The viscosity η_0 in the low-density limit has been measured below 4·2 K (Becker, Misenta & Schmeissner 1954*a*, *b*) and above 14 K (Becker & Misenta 1955).

Estimates of η_0 based on these data and an interpolation between them are given in table 2. Below 6 K, the error due to the interpolation is unlikely to exceed $\pm 0{\cdot}5$ μP. For the original viscosity data an accuracy of better than 1 % was claimed by the authors.

The dependence of η upon the density in the low density limit can be estimated from the modified Enskog theory (MET). This theory successfully predicts the initial density dependence of the thermal conductivity of gaseous ^{4}He (Ahlers 1978) and is also consistent with viscosity measurements for $\rho < 0{\cdot}015$ g cm^{-3} (Van Itterbeek *et al.* 1953). We have (Hirschfelder *et al.* 1967)

$$\frac{\eta}{\eta_0} = \frac{b_0}{V}(y^{-1} + 0{\cdot}8 + 0{\cdot}761y + \ldots), \tag{6.4}$$

where b_0 and y can be obtained from the equation of state of the gas. Using the virial equation

$$\frac{PV}{RT} = 1 + \frac{B}{V} \tag{6.5}$$

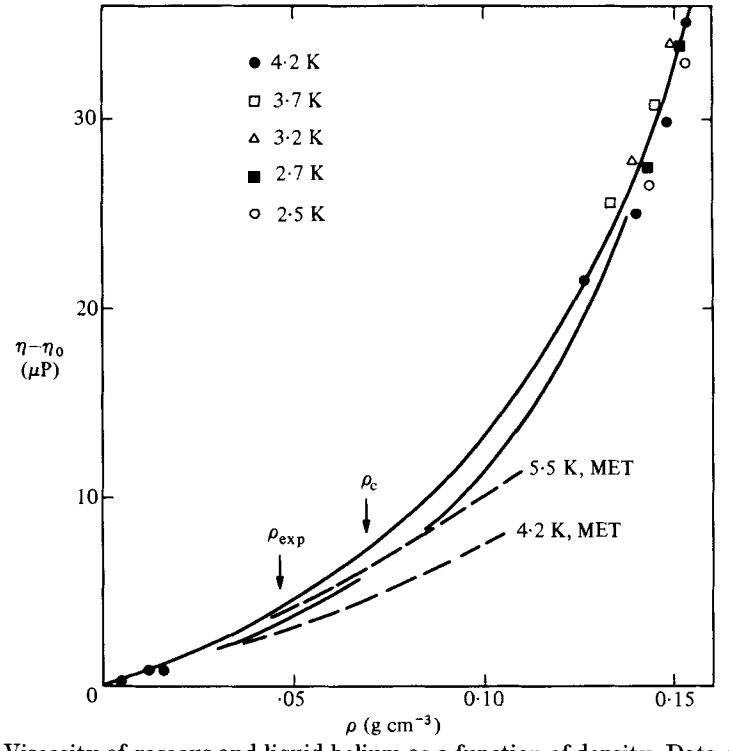

FIGURE 8. Viscosity of gaseous and liquid helium as a function of density. Data are from Goodwin (1968). ---, Modified Enskog theory (MET); ——, interpolation between the MET prediction and the large-ρ data.

with (Keller 1969)

$$B = \alpha + \frac{\beta}{T}, \tag{6.6}$$

where $\alpha = 23{\cdot}05$ cm^3 mol^{-1}, $\beta = -421{\cdot}17$ cm^3 K mol^{-1}, we obtain

$$y = \frac{\alpha}{V}, \tag{6.7}$$

$$b_0 = \alpha. \tag{6.8}$$

Thus

$$\frac{\eta}{\eta_0} = 1 + 0{\cdot}8\frac{\alpha}{V} + 0{\cdot}761\left(\frac{\alpha}{V}\right)^2 + \ldots$$

$$= 1 + 4{\cdot}61\rho + 25{\cdot}2\rho^2 + \ldots, \tag{6.9}$$

where

$$\rho = \frac{4{\cdot}0038}{V} \text{ g cm}^{-3}.$$

The corresponding prediction for $\eta - \eta_0$ is shown as dashed lines in figure 8 for $T = 4{\cdot}2$ K and 5·5 K.

We do not expect the MET to be adequate to predict η at densities as high as 0·05 g cm^{-3}, and we therefore use the viscosity data at liquid densities to estimate departures from the MET. Results for large ρ are available for $T \lesssim 4{\cdot}2$ K (Tjerkstra 1952; Goodwin 1968) and some of the results from Goodwin (1968) are plotted as individual points in figure 8. The excess viscosity $\eta - \eta_0$ is only a weak function of temperature and primarily dependent upon the density. We thus expect that the

Cell	A	B	C	C	D
T_2 (K)	2·1841	2·1841	5·171	5·444	4·515
ρ (g cm^{-3})	0·1462	0·1462	0·045	0·045	0·1250
λ (erg s^{-1} cm^{-1} K^{-1})	1667	1667	—	—	2221
$10^{-7}C_p$ (erg g^{-1} K^{-1})	5·05	5·05	—	—	5·28
$10^6\eta$ (P)	25·6	25·6	17·1	17·8	31·1
$10^4\kappa$ (cm^2 s^{-1})	2·26	2·26	0·86	1·35	3·36
$10^4\nu$ (cm^2 s^{-1})	1·75	1·75	3·80	3·96	2·49
σ	0·78	0·78	4·4	2·9	0·74
d^2/κ(s)	311	297	5·6	3·6	23·0

TABLE 3. Fluid properties

results for $T \lesssim 4{\cdot}2$ K that are shown in figure 8 also represent the viscosity adequately near 5·4 K, and interpolate between the MET prediction and the high-density data as shown by the solid lines in the figure. At the densities of interest this procedure probably does not result in errors larger than 1 μP.

In order to obtain an estimate of the thermal diffusivity κ at the temperature and density used with cell C, we measured the thermal diffusion time of cell A using thermal gradients that yield gravitationally stable density gradients. This was done by raising T_2 by an increment δT_2 as quickly as possible and by measuring the subsequent thermal relaxation of T_1. For a step in T_2 when $t = 0$, we expect $\Delta T'$ for a laterally infinite system to respond according to

$$\Delta T' = -\frac{4}{\pi}\delta T_2 \sum_{i=1}^{\infty} \frac{(-1)^i}{2i-1} \exp\left[-(2i-1)^2 \frac{t'}{\tau}\right], \tag{6.10}$$

where $\tau = 4d^2/\pi^2\kappa$. We have not solved the heat-flow equation for a finite system with lateral boundaries, and for the finite system the behaviour might be slightly different. However, we found that the data with $t' \gtrsim \tau$ could be fitted extremely well by a single exponential in the sum, and that retaining as many as four terms changed the result for τ less than one part in 10^4. We tested this method of measuring κ on the vapour-pressure curve for $T \lesssim 4{\cdot}8$ K, where we know κ independently. We found that the measured values had a precision of 1 %, but were systematically too low by about 15 %. We believe this effect to be caused by the thermal mass of the fluid contained in the annular groove of the bottom copper plug of the convection cell (see figure 4) (the solid material of the bottom of the cell has a negligible heat capacity). We corrected the measurements near 5·2 K for this systematic error but none the less regard the determination of κ as uncertain by perhaps as much as 10 %. Thus our overall accuracy for the Prandtl numbers for the fluid used in cell C is not better than about ± 20 %.

The fluid properties at the operating temperatures and densities of the cells are summarized in table 3.

Properties of ^{4}He at saturated vapour pressure have been reviewed recently also by Barenghi, Lucas & Donnelly (1981).

6.2. *Rayleigh numbers*

The Rayleigh numbers for cells A and B deduced from the measured $\Delta T'$ and the fluid properties discussed in §6.1 have an uncertainty of about 10 %, primarily because of the uncertainty in η. For cell C we do not know the fluid properties well enough to warrant calculating R at all. We therefore present most of our results as

a function of ΔT. For a Boussinesq system, this parameter is equal to R/R_c. For a system with mild departures from the Boussinesq approximation, the small difference between R/R_c and ΔT can be calculated from the fluid properties. In this case, it is best to choose the static temperature at the half height of the cell as a reference temperature T_0 for calculating R/R_c, because then R_c and the initial slope of the Nusselt number as a function of R do not depend upon departures from the Boussinesq approximation to first order (Busse 1967*a*; Ahlers 1980*a*; Walden & Ahlers 1981). In our case, the thermal conductivity was always essentially constant over the small temperature range between T_2 and T_1, and therefore $T_0 = \frac{1}{2}(T_2 + T_1)$. Thus we have

$$\frac{R}{R_c} = \Delta T \frac{\beta_p(T_0)\,\kappa(T_{0c})\,\nu(T_{0c})}{\beta_p(T_{0c})\,\kappa(T_0)\,\nu(T_0)}, \tag{6.11}$$

where T_{0c} is the value of T_0 when $\Delta T = 1$. For the temperature used with cells A and B, the experimental values of the fluid properties yield

$$\frac{R}{R_c} = \Delta T(1 + 0{\cdot}0305\epsilon' - 3{\cdot}8 \times 10^{-4}\epsilon'^2) \tag{6.12}$$

for $\Delta T \lesssim 15$. Here $\epsilon' = \Delta T - 1$.

Departures from the Boussinesq approximation can be expressed in terms of a parameter Q defined by Busse (1967*a*). For cells A and B, $Q = -0{\cdot}20$ when $\Delta T = 1$, and previous work on non-Boussinesq samples (Ahlers 1980*a*; Walden & Ahlers 1981) indicates that the results for such a small value of Q should correspond to the Boussinesq system.

7. Results

7.1. *Critical Rayleigh numbers*

The temperature differences $\Delta T'_c$ at onset of convection were determined by measuring the Nusselt number N in the vicinity of the convective onset. Either a graphical extrapolation of N for $\Delta T' > \Delta T'_c$, or a least-squares fit as described in §7.3, yielded $\Delta T'_c$ with high precision. We found

$$\Delta T'_c = 599{\cdot}6 \pm 4\ \mu\text{K} \tag{7.1a}$$

for cell A, and

$$\Delta T'_c = 676{\cdot}2 \pm 8\ \mu\text{K} \tag{7.1b}$$

for cell B. The uncertainties are due almost entirely to the uncertainty in $\Delta T'_0$ (see figure 7), which is caused by variations in the small background heating. The values of the critical Rayleigh numbers R_c, calculated at the horizontal midplane of the cells, are

$$R_c^A = 1599 \pm 240 \tag{7.2a}$$

for cell A, and

$$R_c^B = 1694 \pm 250 \tag{7.2b}$$

for cell B. The uncertainties in R_c are due primarily to uncertainties in the fluid properties (especially in the viscosity) and to a lesser extent to the cell height d. The ratio R_c^B/R_c^A is known much more accurately because it contains error contributions only from $\Delta T'_c$ and from d. Thus

$$\frac{R_c^B}{R_c^A} = 1{\cdot}059 \pm 0{\cdot}02. \tag{7.3}$$

For cell C, which was operated near 5 K and at densities near 0·05 g cm^{-3}, $\Delta T'_c$ depended sensitively on the precise density and temperature. We do not know the fluid properties well enough to calculate Rayleigh numbers in that region of the phase diagram.

For a laterally infinite system with rigid, perfectly conducting upper and lower boundaries, we expect $R_c^\infty = 1708$ (see e.g. Chandrasekhar 1961). But for the finite system $R_c > R_c^\infty$ and depends upon L, the symmetry of the convective flow pattern, and the boundary conditions at the lateral walls. For our cells, numerical estimates (Sparrow, Goldstein & Jonsson 1964; Nield 1968; Steinberg, private communication) show that the upper and lower boundaries may be considered as perfect conductors. For the lateral walls, three types of boundary conditions have been explored theoretically. Brown & Stewartson (1978) considered the case of so-called 'imperfectly insulating' sidewalls corresponding to walls of non-vanishing conductivity and imperfect thermal attachment to the top and/or bottom plate. This case leads to lateral heat flow even in the absence of convection and therefore results in an imperfect bifurcation. Our walls are thermally well attached (see §2.3.1), and we find that the convective onset is sharp (see §7.2). Therefore the boundaries of Brown & Stewartson's case do not pertain to our experiment. The other two cases correspond to walls that are thermally well attached at the top and bottom plate but have either zero or infinite thermal conductivity. They are referred to as 'insulating' or 'conducting' sidewalls, and both have been used in the calculations by Charlson & Sani (1970, 1971, 1975). The real system is, of course, always an intermediate case, and the appropriate boundary conditions have been discussed by Cross *et al.* (1983) (see their equations (B 7) and (B 8)) and by Cross *et al.* (1980). For any of these cases, a sharp bifurcation is expected at R_c; but calculations of R_c have been carried out so far only for the two extremes (Charlson & Sani 1970). The results indicate that, for our aspect ratios, the value of R_c is not very sensitive to the nature of the boundaries. The initial slope of the Nusselt number (Charlson & Sani 1975), however, differs a lot for the two extremes. The insulating case agrees with the measurements (see §7.3) remarkably well, suggesting that the real walls are closer to 'insulating' than to 'conducting'. Therefore we shall compare our data with the calculations for insulating walls.

For insulating walls, $R_c(L)$ has been obtained numerically by a variational calculation for axisymmetric flow (Charlson & Sani 1970), and for non-axisymmetric flow with radial nodes (Charlson & Sani 1971). For axisymmetric flow, $R_c(4{\cdot}72) = 1734$ and $R_c(2{\cdot}08) = 1840$. But the variational calculations for non-axisymmetric flow (Charlson & Sani 1971) indicate that the critical Rayleigh numbers for certain non-axisymmetric states are not much different (the stability of non-axisymmetric solutions has been investigated only to a very limited extent: see Charlson & Sani 1975). Clearly the experimental uncertainties in R_c^A and R_c^B are so large that the measurements cannot distinguish between R_c^∞ and the calculations for the finite system. However, the *ratio* R_c^B/R_c^A is more accurate and in remarkably good agreement with the variational calculation, which yields 1·061, with uncertainties, however, that are hard to estimate. The calculated values of $R_c(L)$ for $L \lesssim 3$ are also in good agreement with the experimental values of Stork & Müller (1975), which were obtained with essentially insulating sidewalls (note that Stork & Müller's h is equal to $2L$). Our investigation thus extends the comparison with the variational calculations to larger L.

The increase in R_c due to the lateral boundaries can also be calculated from the

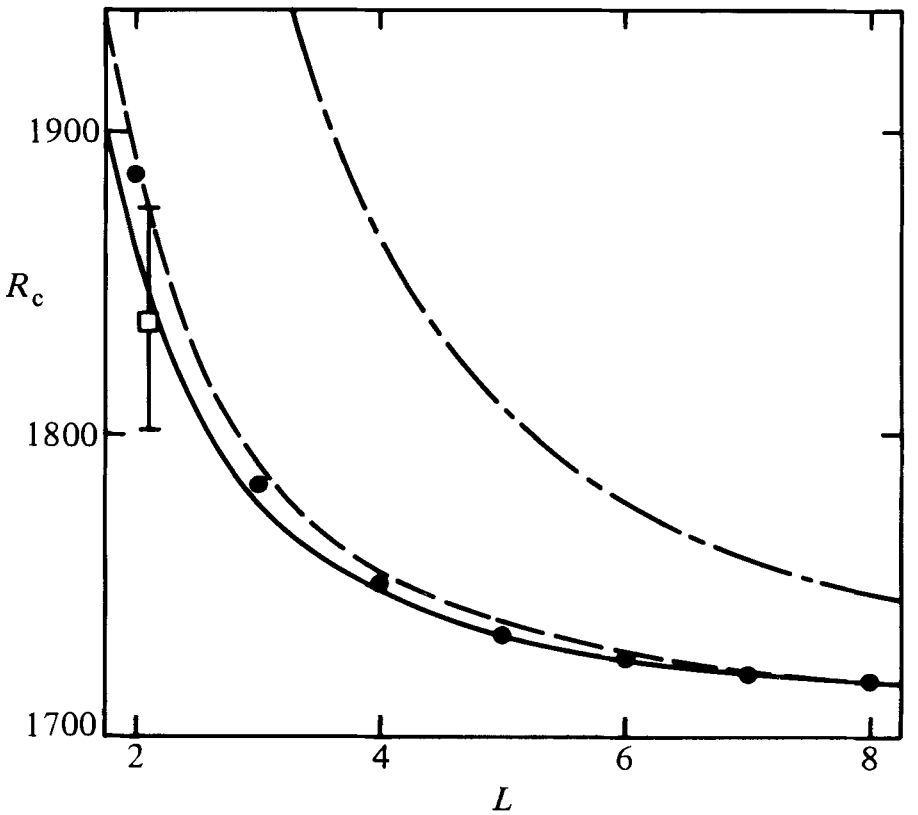

FIGURE 9. Critical Rayleigh numbers as a function of aspect ratio L. ●, Charlson & Sani (1970), axisymmetric flow with finite centre amplitude and conducting side walls; ——, Ahlers *et al.* (1981), axisymmetric flow with finite centre amplitude; – – –, Ahlers *et al.* (1981), straight rolls; -—·—, Ahlers *et al.* (1981), concentric rolls with vanishing centre amplitude; □, experimental result for R_c^B/R_c^A, normalized to the solid line at $L = 4{\cdot}72$ (cell A).

amplitude equation (Ahlers *et al.* 1981) for the lowest mode that contributes to the shape of the convective flow immediately above R_c. That equation yields a shift

$$\epsilon_c = \frac{R_c - R_c^\infty}{R_c^\infty} \tag{7.4}$$

that depends upon the symmetry of the convective flow. For the case of cylindrically symmetric flow with a finite amplitude at the centre of the cell, one has

$$\epsilon_c = \frac{\pi^2 \xi_0^2}{4L^2}, \tag{7.5}$$

where $\xi_0^2 = 0{\cdot}148$. This prediction, in the form of $R_c(L)$, is shown as a solid line in figure 9. Also shown, but as solid circles, are the calculations by Charlson & Sani (1970) for conducting lateral walls (insulating walls give results that are non-monotonic in L and slightly lower at some values of L: see Charlson & Sani 1970). These results correspond to finite amplitudes at the cell centre, and thus should be directly comparable with the prediction (7.5). The agreement is seen to be excellent for all $L \gtrsim 2$. *A priori* one would have expected some discrepancy for small L, because the amplitude equation is based upon the assumption of slow spatial variations and therefore strictly applicable only for large L.

The amplitude equation has the virtue that it can be applied relatively easily to a number of flow symmetries. Thus, it has been suggested (Brown & Stewartson 1978) that the amplitude at the centre of a cylindrically symmetric flow vanishes if L is sufficiently large. For that case, one obtains (Ahlers *et al.* 1981)

$$\epsilon_c = \frac{\pi^2 \xi_0^2}{L^2}, \tag{7.6}$$

a shift that is four times larger than the shift for a finite amplitude at the centre. This prediction is shown as a dash–dotted line in figure 9. Finally, the experiments of Stork & Müller suggest that the stable flow pattern for their ratios $L \leqslant 3{\cdot}2$ and insulating walls consists of straight, parallel rolls (see also Kirchartz *et al.* 1981). For that case, one obtains from the amplitude equation

$$\epsilon_c = \frac{1{\cdot}18\pi^2 \xi_0^2}{4L^2}. \tag{7.7}$$

This is shown as a dashed line in figure 9, and is numerically so similar to the case of concentric rolls with finite centre amplitude that at present we cannot hope to distinguish experimentally between these two cases.

The experimental values (7.2*a*, *b*) of R_c do not distinguish between the results summarized in figure 9, except for the value of R_c for $L = 2{\cdot}08$ (7.2*b*), which disagrees with the prediction for concentric rolls and zero centre amplitude. Although *a priori* we do not expect the amplitude equation to be accurate for small L, the success for the case of finite centre amplitude suggests that the comparison between experiment and the result (7.6) may be valid, and that a concentric flow pattern with zero centre amplitude did not exist in the $L = 2{\cdot}08$ cell. This would be consistent with the expectations based on the work of Brown & Stewartson (1978), which suggests that the centre amplitude for cylindrically symmetric flow should grow with decreasing L as $(\ln L)^{-\frac{1}{2}}$.

A more sensitive comparison between theory and experiment can be obtained with the ratio (7.3). Normalizing $R_c(4{\cdot}72)$ to the results of Charlson & Sani (1970), and (7.3), yield the open square in figure 9 for $R_c(2{\cdot}08)$. That result is consistent with either cylindrically symmetric rolls and finite centre amplitude, or with straight and parallel rolls.

7.2. *Sharpness of the convective onset at* R_c

The onset of convection in ideal, flat, horizontal fluid layers is expected to be sharp, even if the layer is of finite lateral extent. Nonetheless, early measurements in cell D (see table 1) revealed some rounding of the Nusselt number $N(R)$ near R_c (Ahlers 1974, 1975, 1980*a*). Some of those data are shown in figure 10 as open circles. They yield $N(R_c) - 1 \approx 0{\cdot}03$. The rounding could be caused for instance by a non-horizontal alignment of the fluid layer, by non-parallelism of the top and bottom plates, or by lateral heat flow into imperfectly insulating sidewalls (Daniels 1977; Hall & Walton 1977; Reiss 1977; Brown & Stewartson 1978; Kelly & Pal 1978; Tavantzis *et al.* 1978). Cell D was not as carefully constructed as cells A, B and C, and its height d may have been non-uniform by as much as 3% (Ahlers 1978). Cells A and B are believed to have fluid-layer thicknesses that vary by only $0{\cdot}3 \pm 0{\cdot}3$% (see table 1). Results for cell A are shown in figure 10 as solid circles. They reveal a transition that is an order of magnitude sharper than the transition for cell D, with $N(R_c) - 1 \approx 0{\cdot}002$. A more detailed plot of the data for cell A is shown in figure 14 of Ahlers *et al.* (1981). Results for cell B ($L = 2{\cdot}08$), although not shown in figure 11, showed a convective

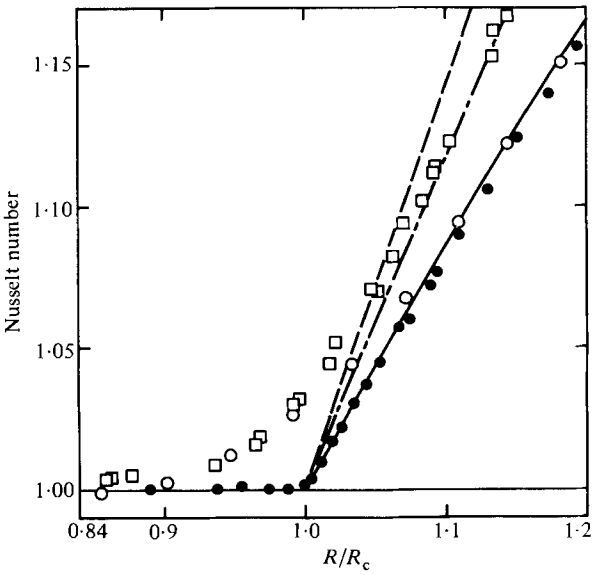

FIGURE 10. Nusselt numbers near the onset of convection. ●, Cell A; ○, cell D; □, cell C; ——, fit to cell D data with $R \geqslant 1{\cdot}1R_c$ (Ahlers 1980*a*, *b*); – – –, prediction for the laterally infinite system (Schlüter *et al.* 1965); -·-·-, fit to cell C data with $R \geqslant 1{\cdot}1R_c$ (table 4).

onset nearly as sharp as that for cell A. Since all of the cells had rather similar walls, made of thin stainless steel, and, since the horizontal alignment was equally good for all of them, we conclude that the rounding in cell D was caused primarily by variation in the height of the fluid layer.

Cell C ($L = 57$) had a much smaller height (table 1) than cells A and B. Therefore the same degree of parallelism of the top and bottom plates corresponded to a greater relative variation in the cell height. Indeed, the rounding near R_c was an order of magnitude greater than for cells A and B, and about equal to the rounding of cell D. Data for cell C are shown in figure 10 as open squares.

The very small rounding in cell A (which is only slightly larger than the experimental resolution) has been compared (Ahlers *et al.* 1981, figure 14) with the rounding that would be produced by a small inhomogeneous term in the amplitude equation for the evolution of convective flow. An inhomogeneous term, either deterministic or stochastic in character, of the size needed to explain the timescale for the convective onset when R is swept through R_c, is also adequate to explain the rounding for cell A.

7.3. *Nusselt numbers near* R_c

Measurements very near R_c were particularly difficult because of the slowness of approach towards a steady state (for this critical slowing down see Behringer & Ahlers 1977). For cells A and B, they were made under full computer control, with the sequence of events for each 'point' as shown in figures 6 and 7. The temperature difference with zero applied power, and the thermal conductivity with $\Delta T \approx 0{\cdot}87$, were determined before and after each measurement to minimize effects of drifts and maximize the precision. A slow ramp, $dq/dt \approx 2 \times 10^{-2}$, in heater power was used, starting at $\Delta T \approx 0{\cdot}87$, to enter the convecting state. Upon reaching the desired power, that power was maintained for two to five hours (depending upon the closeness of R_c) and the evolution of the temperature difference was monitored.

For cell C, measurements were relatively easier because of the smaller vertical

thermal diffusion time. In addition, the larger 'rounding' near R_c (see §7.2) made measurements *very* near R_c meaningless. Most of the measurements for cell C were made manually, by increasing or decreasing q in small steps.

Theoretical predictions for the convective heat transport are often presented in terms of the initial slope N_1 of N near R_c. In order to obtain objective experimental values of N_1, we fitted data to the equation

$$N-1 = \sum_{i=1}^{k} N_i \bar{\epsilon}^i \tag{7.8}$$

with

$$\bar{\epsilon} = \frac{R-R_c}{R_c}. \tag{7.9}$$

In these fits, the coefficients N_i *and* the critical Rayleigh number R_c were least-squares adjusted.

Equation (7.8) was usually truncated at $k = 2$ or 3. In order to assess the effect of this truncation, we fitted the data also to the equation

$$\frac{(N-1)R}{R_c} = \sum_{i=1}^{k} \tilde{N}_i \bar{\epsilon}^i. \tag{7.10}$$

In the absence of truncation errors we would expect

$$\tilde{N}_1 = N_1, \tag{7.11a}$$

$$\tilde{N}_2 = N_1 + N_2, \tag{7.11b}$$

$$\tilde{N}_3 = N_2 + N_3. \tag{7.11c}$$

Thus we regard any difference between N_1 and $\tilde{N}_1$ as an indication of systematic errors due to the finite number of terms in (7.8) or (7.10).

In order to indicate the quality of the fit, we also present in each case the standard error

$$p = \left[\frac{\sum_{i=1}^{n} (N_i - N_i^{\text{fit}})^2}{n-k-1}\right]^{\frac{1}{2}}. \tag{7.12}$$

Here n is the number of data points.

Our final estimates of N_1 for all cells, as well as for data obtained by Koschmieder & Pallas (1974), together with somewhat subjective estimates of their uncertainties, are given in table 4. We now discuss in detail how these results were obtained.

7.3.1. *Cell B* ($L = 2{\cdot}08$). Typical results for the dimensionless convective heat transport $q-\Delta T$ during the period of steady heating after the ramp are displayed in figure 11. The time origin for this figure is at the beginning of the ramp, although the ramp period is not shown. The time span covered by the figure corresponds to about $2\frac{1}{2}$ h. For relatively small $q-\Delta T$, such as for the data labelled (*A*), $q-\Delta T$ has attained a value that is constant within experimental noise at rather early times. This steady-state value is equal to $(N-1)R/R_c$. For larger $q-\Delta T$ the temporal evolution of $q-\Delta T$ is more complicated. A plateau forms for $t \gtrsim 10$; but this corresponds to an unstable state, labelled (*a*), which with increasing time decays in favour of state (*b*), which has associated with it a larger convective heat transport. As can be seen from figure 11, the lifetime of state (*a*) decreases as $q-\Delta T$ increases, but the data are not good enough to make a more quantitative statement. Even when state (*a*) is unstable, it is still possible to obtain $(N-1)R/R_c$ for state (*a*) by using the value of $q-\Delta T$ in the plateau region. The long-time limit of $q-\Delta T$ gives $(N-1)R/R_c$ for

Cell	L	N_1
B (a)	2·08	0·36 ± 0·04
B (b)	2·08	0·35
A (unstable)	4·72	0·56 ± 0·06
A (stable)	4·72	0·83 ± 0·02
D	5·27	0·96 ± 0·06
C	57	1·25 ± 0·05
K+P	13	1·3 ± 0·3

TABLE 4. Initial slopes of the Nusselt number $N(R)$ (see (7.8)–(7.11)

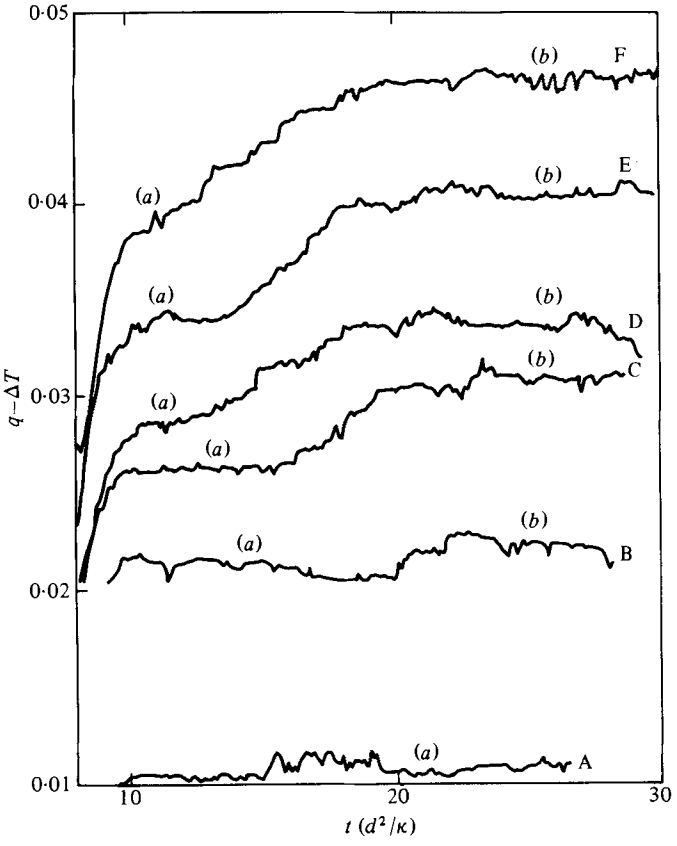

FIGURE 11. The convective heat transport $q-\Delta T$ as a function of time for cell B. Note the intermediate state (a), which decays to state (b) for large t.

state (b). From a large number of measurements as described above we determined that state (a) is unstable and decays to state (b) for $R > 1{\cdot}04\,R_c$. For smaller R, the difference between $q-\Delta T$ for the two states becomes too small to be measurable. Thus, we assumed initially, and cannot rule out, that state (b) is the result of a bifurcation at $R_b \approx 1{\cdot}04 R_c$. Further analysis of the data, to be discussed below, suggests, however, that state (b) is stable for all $R > R_c$, and that the difference in $q-\Delta T$ for states (a) and (b) vanishes at R_c as $\bar{\epsilon}^2$ and becomes of the same order as the experimental resolution for $\bar{\epsilon} \approx 0{\cdot}04$. The Nusselt-number results for states (a) and (b) are shown in figure 12.

We investigated the effect of the ramp rate $\beta = dq/dt$ that was used to enter the

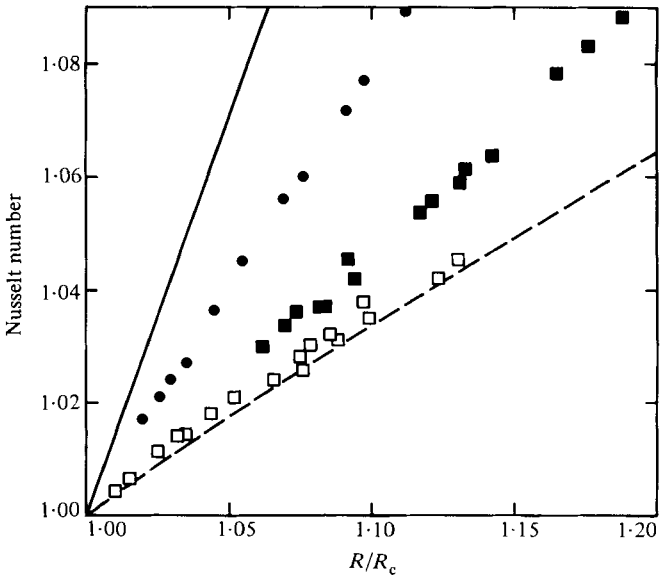

FIGURE 12. Nusselt numbers for cells A and B near the convective onset. □, Cell B, state (*a*) (see figure 11); ■, cell B, state (*b*) (see figure 11); ●, cell A, stable state (also shown in figures 10 and 13 for comparison); ——, prediction for laterally infinite system (Schlüter *et al.* 1965); – – –, Charlson & Sani (1965) for $L = 2{\cdot}25$, concentric rolls with finite centre amplitude.

convecting state by varying β over the range 0·01–0·045. This was done with a final power level that yielded $q - \Delta T = 0{\cdot}060$ and state (*b*). The ramp rate had no influence on $q - \Delta T$ in the final state. However, when β was very small, the plateau corresponding to the unstable state (*a*) was not observed. Instead, the shape of $q - \Delta T$ during the ramp revealed that (*a*) was decaying to (*b*) prior to attainment of the steady-state power level.

In figure 12, we compare the measured values of N with those calculated by Charlson & Sani (1975) for axisymmetric flow with non-conducting lateral walls and $L = 2{\cdot}25$ (dashed line). The agreement of the state (*a*) data with the theory is excellent, with the small systematic difference of about 0·002 in N possibly caused by a slightly incorrect choice of R_c for the experimental data. Therefore, it appears very likely that an axisymmetric flow, with finite centre amplitude, evolves initially in our cell B. But at a later time it decays in favour of a state of different and presently unknown symmetry. Charlson & Sani, to a limited extent, examined the stability of their axisymmetric flow, and under the conditions that they investigated found it to become unstable for $R >$ (1·04 to 1·1) R_c.

The decay of our state (*a*) is also consistent with the observation made of non-axisymmetric flow by Stork & Müller (1975) in systems of similar aspect ratio. It agrees even more dramatically with the recent observations by Kirchartz *et al.* (1981). These authors found, for $L \approx 3$, that a circular flow pattern with finite centre amplitude evolved initially when the convecting state was entered relatively *rapidly*. This pattern decayed to a non-centrosymmetric one at large times and under stationary external conditions. However, the experiments of Kirchartz *et al.* were performed at rather larger ramp rates and equilibration took place at rather larger values of R. Our measurements suggest that the unstable (presumably circular) state always forms first, even when the convecting regime is entered at very small ramp rates; but for small ramp rates the decay occurs at very small values of $R - R_c$ and possibly during the duration of the ramp.

Fit no.	Cell	$\bar{\epsilon}_{max}$	Equation	N_1 or $\tilde{N}_1$	N_2 or $\tilde{N}_2$	N_3 or $\tilde{N}_3$	$10^3 p$	n
1	B (*a*)	0·1	(7.8)	0·348, 13	0*	0*	1·3	14
2	B (*a*)	0·1	(7.10)	0·389, 14	0*	0*	1·4	14
3	B (*a*)	0·1	(7.8)	0·363, 70	−0·12, 60	0*	1·3	14
4	B (*a*)	0·1	(7.10)	0·361, 80	0·23, 60	0*	1·4	14
5	B (*b*)	0·28	(7.8)	0·372, 60	0·51, 13	0*	3·4	36
6	B (*b*)	0·28	(7.10)	0·321, 90	1·12, 14	0*	3·9	36
7	A	0·1	(7.8)	0·789, 6	0*	0*	0·9	46
8	A	0·1	(7.10)	0·873, 6	0*	0*	0·9	46
9	A	0·1	(7.8)	0·827, 22	−0·36, 21	0*	0·8	46
10	A	0·1	(7.10)	0·830, 24	0·41, 22	0*	0·9	46
11	A	0·28	(7.8)	0·820, 6	−0·21, 3	0*	0·9	63
12	A	0·28	(7.10)	0·829, 6	0·53, 3	0*	1·0	63
13	A	0·5	(7.8)	0·816, 9	−0·22, 2	0*	2·3	77
14	A	0·5	(7.10)	0·837, 12	0·46, 3	0*	3·0	77
15	C (1)	0·5	(7.8)	1·124, 46	−0·47, 8	0*	4·2	23
16	C (1)	0·5	(7.10)	1·244, 64	0·22, 9	0*	5·2	23
17	C (1)	1·0	(7.8)	1·187, 40	−0·66, 10	0·18, 6	3·8	30
18	C (1)	1·0	(7.10)	1·267, 60	0·23, 13	−0·09, 8	5·3	30
19	C (2)	0·5	(7.8)	1·202, 14	−0·62, 3	0*	1·1	22
20	C (2)	0·5	(7.10)	1·348, 19	0·37, 3	0*	1·4	22
21	C (2)	0·5	(7.8)	1·262, 56	−0·85, 22	0·26, 25	1·1	22
22	C (2)	0·5	(7.10)	1·284, 82	0·26, 27	−0·26, 31	1·4	22
23	C (2)	1·0	(7.8)	1·259, 12	−0·86, 3	0·30, 3	1·0	28
24	C (2)	1·0	(7.10)	1·361, 18	0·00, 4	0·03, 3	1·4	28
25	K+P	1·0	(7.8)	1·223, 240	−0·79, 47	0·25, 27	11·8	15
26	K+P	1·0	(7.10)	1·349, 390	0·01, 63	0·01, 36	16·5	15

TABLE 5. Least-squares fitted parameters of (7.8) and (7.10); * indicates parameter held fixed

For comparison, we show in figure 12 as a solid line the prediction of Schlüter, Lortz & Busse (1965) for the laterally infinite system.

A least-squares fit of the data for state (*a*) to (7.8) and (7.10) yielded the results in the first four lines of table 5. In each case, we used data with $\bar{\epsilon} > \bar{\epsilon}_{min}$, $\bar{\epsilon}_{min} = 10^{-2}$, in order to avoid data affected by rounding near R_c (see §7.2). On the basis of these fits, we conclude that $N_1 = 0{\cdot}36$, with an uncertainty of perhaps 10%. This result agrees well with the value 0·35 obtained by interpolating between the results obtained by Charlson & Sani (1975) for $L = 1$ and 2·25 and insulating sidewalls. Charlson & Sani also found that $N_2 < 0$. Whereas our data for state (*a*) are consistent with that, our uncertainty for N_2 is rather large because state (*a*) exists only for small $\bar{\epsilon}$, where $\bar{\epsilon}^2$ is very small. Charlson & Sani's (1975) calculations of N_1 for conducting lateral walls yield $N_1 \approx 0{\cdot}78$ for our L, and thus differ appreciably from the experimental results for either state (*a*) or state (*b*).

All four of the fits for state (*a*) yielded values of R_c in the range 1688 ± 2.

For state (*b*), there are no data with $\bar{\epsilon} < 0{\cdot}04$ that can be distinguished from state (*a*) data. For that reason an analysis with $\epsilon_{max} = 0{\cdot}1$ would have included too few data points to be meaningful. Thus we used $\epsilon_{max} = 0{\cdot}28$. The results are listed as fits 5 and 6 in table 5. We obtained values for N_1 that are very similar to those for state (*a*); but N_2 is considerably larger than zero, and $N(R)$ curves upwards. The values obtained for R_c are in the range 1680 ± 10, consistent with R_c for state (*a*). The analysis therefore suggests that states (*a*) and (*b*) have the same R_c, but differ in convective heat transport by a term about equal to $0{\cdot}6\bar{\epsilon}^2$. As mentioned above, we

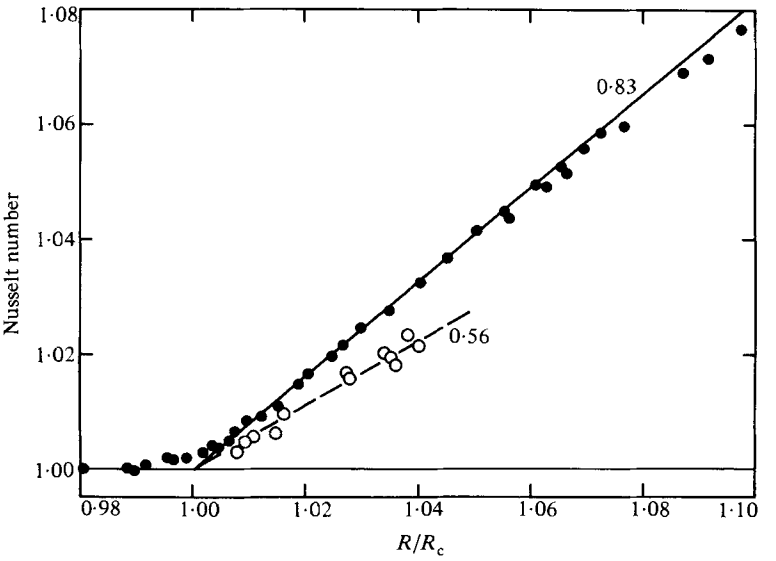

FIGURE 13. Nusselt numbers for cell A near the convective onset. ○, Unstable state; ●, stable state (see also Ahlers *et al.* 1981). The solid and dashed lines are straight and have slopes 0·83 and 0·56 respectively (see table 4).

cannot distinguish between this interpretation on the one hand, and state (*b*) arising as a result of a bifurcation near $R_b \approx 1{\cdot}04R_c$ on the other.

Lastly, let us remark that in a preliminary publication (Behringer & Ahlers 1977) we quoted $N_1 \approx 0{\cdot}48$. At that time, we had indications of complicated behaviour for cell B, but were unaware of the existence of two states, because our data had more scatter. The quoted value for N_1 was the result of a straight-line fit to data primarily for state (*b*), and with $\bar{\epsilon} \lesssim 0{\cdot}2$. Our more precise data for state (*b*), when analysed in the same way, give a similar result (cf. figure 12).

7.3.2. *Cell A* ($L = 4{\cdot}72$). The time evolution of the convective heat transport in cell A has been discussed in great detail by Ahlers *et al.* (1981). For this cell, an unstable state forms initially and decays at a later time to a final steady state. Results for $N(R)$ for both the stable and the unstable state are shown in figure 13. The unstable state is sufficiently long-lived for $N(R)$ to be measurable only when $\bar{\epsilon} \lesssim 0{\cdot}04$. This can be compared with state (*a*) of cell B, which was observable for $\bar{\epsilon}$ as large as 0·13 (see figures 11 and 12). Because of the narrow existence range of the unstable state for cell A, a detailed analysis of $N(R)$ is not justified, and we simply estimate N_1 on the basis of the dashed straight line in figure 13. We find $N_1 = 0{\cdot}56 \pm 0{\cdot}06$. This value is consistent with a linear extrapolation of the Charlson & Sani (1975) results for concentric rolls with finite centre amplitude as shown in figure 14. An actual calculation of N_1 for L near 4·72 would of course be very useful for comparison with the experiment.

The stable state for cell A has been analysed in detail by fitting to (7.8) and (7.10), and the results are given in lines 7–14 of table 5. On the basis of that analysis, we conclude that $N_1 = 0{\cdot}83 \pm 0{\cdot}02$ and $N_2 \simeq -0{\cdot}3 < 0$. The work of Stork & Müller (1975) and Kirchartz *et al.* (1981) at somewhat smaller values of L suggests that the stable state should consist of a set of parallel, straight rolls. For that flow symmetry, and cylindrical boundary conditions, one obtains $N_1 = 0{\cdot}73$ from the amplitude equation (Ahlers *et al.* 1981). This is slightly lower than the experiment, but perhaps not entirely inconsistent if allowance is made for slight deviations near the walls from

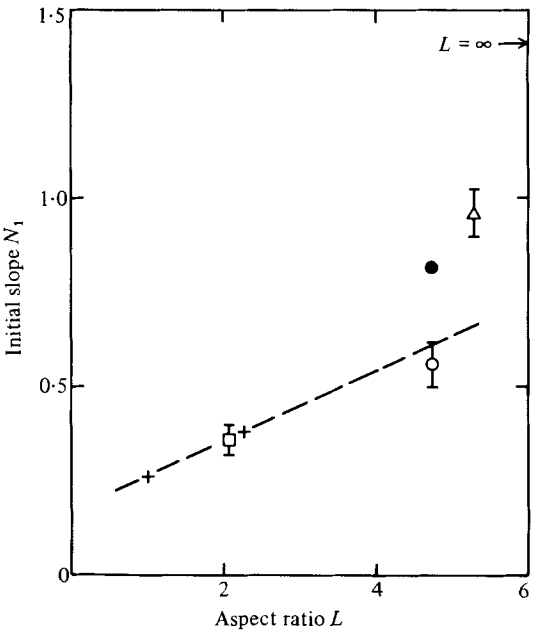

FIGURE 14. Initial slopes N_1 of $N(R)$ (see (7.8)) as a function of aspect ratio L. +, Charlson & Sani (1975), concentric rolls with finite centre amplitude; □, cell B, state (*a*); ○, cell A, unstable; ●, cell A, stable; △, cell D. The dashed line is straight and drawn through the Charlson & Sani results.

the assumed flow geometry. Alternately, the work of Koschmieder & Pallas (1974) suggests that the flow should consist of concentric rolls, but possibly with a vanishing amplitude at the centre. For that case, the amplitude equation yields $N_1 = 0{\cdot}85$, which is also quite consistent with the experiment. This latter interpretation was adopted in the work of Ahlers *et al.* (1981), although their conclusions are largely independent of the assumed flow pattern. As discussed in §7.1, it is inconsistent with the shift in R_c due to the finite geometry. An interpretation in terms of straight rolls as observed by Stork & Müller is thus more nearly consistent with all our experimental observations.

For comparison, we have also shown in figure 14 (as an open triangle) the result for N_1 of cell D, as reported by Ahlers (1980*a*).

7.3.3. *Cell C* ($L = 57$). For cell C, there is considerable rounding near R_c, as shown in figure 10. We therefore excluded all data with $\bar{\epsilon} < 0{\cdot}1$ from any data analysis. Already in the rounded region, the flow in this cell became non-periodically time-dependent (Ahlers & Behringer 1978*a*, *b*). To illustrate this, we show in figure 15 as open triangles and as a function of R/R_c the experimentally measured standard deviation from the mean of N:

$$p_N = \langle (N(t) - \langle N \rangle)^2 \rangle^{\frac{1}{2}}.$$

Here the angle bracket indicates a time average, typically over a two hour period. The data near $R/R_c = 0$ (note the break in the abscissa) represent the instrumental noise level of about $2{\cdot}5 \times 10^{-4}$, and provide a baseline to judge whether the fluid flow is noisy. Clearly, at $R/R_c = 0{\cdot}8$ there is no measurable fluid noise; but at $R/R_c = 1$ the noise from the fluid already exceeds the instrumental noise level by 20%. Also shown, as solid triangles, are values of $\langle N \rangle$. They show the rounding in the range $0{\cdot}9 \lesssim R/R_c \lesssim 1{\cdot}1$ that was discussed in §7.2.

Time-average measurements of N were made at two different temperatures (5·171

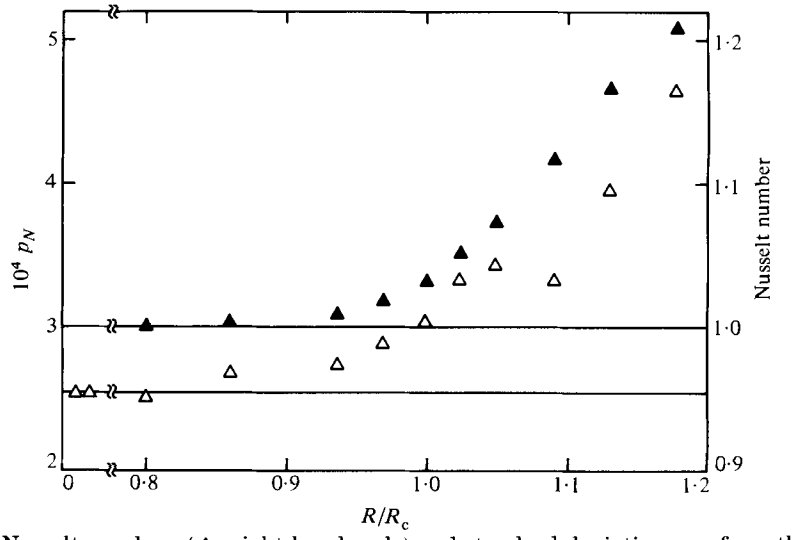

FIGURE 15. Nusselt numbers (▲, right-hand scale) and standard deviations p_N from the mean of the (time-dependent) Nusselt number (△, left-hand scale) near the convective onset for cell C.

and 5·444 K, see table 3). They are identified as sets 1 and 2 respectively. The results of least-squares fits to (7.8) and (7.10) with $\bar{\epsilon}_{\max} = 0{\cdot}5$ and 1·0 for the two sets are given in lines 15–24 of table 5. They yield $N_1 \approx 1{\cdot}25$, with an uncertainty of about $\pm 0{\cdot}05$. For the second coefficient we get $N_2 \approx -0{\cdot}6$. Although it is hard to estimate the uncertainty in N_2 (it perhaps is not larger than $\pm 0{\cdot}2$), we feel that N_2 is definitely negative.

One might have expected the large-aspect-ratio system to agree with the theory for $L = \infty$. For that case, a set of straight rolls and $\sigma = 3$ yields $N_1 = 1{\cdot}431$ (Schlüter *et al.* 1965), definitely larger than the experimental result. This difference is of course not surprising since our fluid flow is time-dependent and thus cannot correspond very closely to parallel, straight rolls.

The measurements by Koschmieder & Pallas (1974) in a cylindrical cell with $L = 13$ have been interpreted by those authors to yield $N_1 = 1{\cdot}48$, in agreement with the theory for straight rolls. We have analysed their data by fitting them to (7.8) and (7.10), with $\bar{\epsilon}_{\max} = 1$ and $\bar{\epsilon}_{\min} = 0{\cdot}1$. For this purpose, we used a combination of data (Pallas 1972) taken on oils of viscosity $\eta = 100$ and 200 cSt (there appeared to be no noticeable systematic differences between the two sets of data, and any one set had only relatively few points in the range of $\bar{\epsilon}$ used). The results are shown in lines 25 and 26 of table 5. We found that our least-squares fit gave an R_c that was about 5% lower than the value adopted by the original authors, and an initial slope of about $1{\cdot}3 \pm 0{\cdot}3$. Thus, our interpretation of the Koschmieder & Pallas results does not distinguish between the theoretical results (Schlüter *et al.* 1965) for rolls, squares or hexagons in a laterally infinite system.

7.4. *Nusselt numbers at larger R*

For cells A and C, $N(R)$ was measured for $R/R_c \lesssim 24$ and $R/R_c \lesssim 2{\cdot}3$ respectively. Over that range, $N(R)$ increased monotonically, was concave downward, and had no singularities that were detectable within our resolution. Representative results are shown in figure 16 for $R/R_c \leqslant 2{\cdot}4$. The absence of singularities agrees with earlier measurements by Koschmieder & Pallas (1974) and by Ahlers (1974, 1975, 1980*a*). The results for cell A were similar to, but very slightly lower than, the measurements

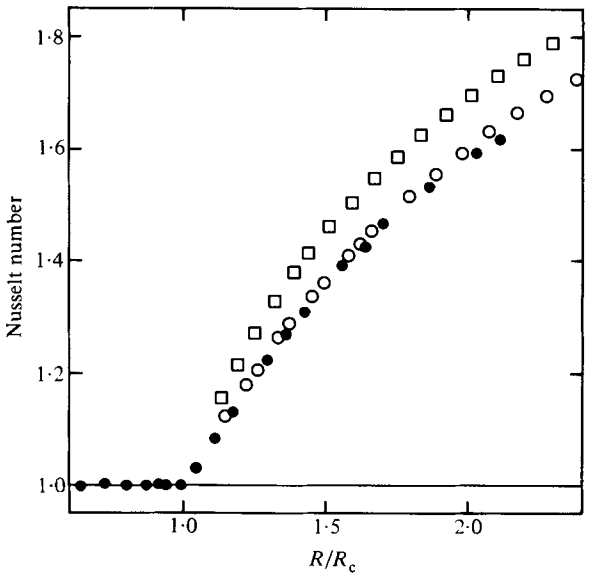

FIGURE 16. Nusselt numbers over a wider range of Rayleigh numbers for cells A (●), D (○), and C (□).

for cell D that were reported by Ahlers (1974, 1975, 1980*a*). Results for cell D (Ahlers 1980*a*) are shown in figure 16 for comparison.

The behaviour of cell B ($L = 2{\cdot}08$) at large R was much more complicated, and we discuss it here in some detail. A series of heat-transport measurements was made for $R/R_c \lesssim 12$, using the manual technique of increasing or decreasing the heater current in small steps and waiting for a steady-state temperature difference to be reached after each step. Occasionally, the heater current was reduced to zero to confirm the absence of drifts in the apparatus. Results of these measurements are shown in figure 17. Aside from the onset of fluid flow at $R/R_c = 1$, the most dramatic feature displayed by the data is the discontinuous decrease in N near $\Delta T \approx 3$. A second transition occurs in the range $8 \lesssim \Delta T \lesssim 9$, and has a wide hysteresis loop associated with it. Let us first discuss the transition near $\Delta T = 3$.

Upon increasing the Rayleigh number, the system remains in state (*b*) for $\Delta T \lesssim 3$. As can be seen from figure 17, the system then undergoes a transition, which manifests itself by a large, discontinuous *decrease* in the convective heat transport. We shall label the new state as state (*c*). The transition was investigated in detail first by the usual technique of applying a constant heat current and measuring the resulting temperature difference. These results are shown as solid symbols in figure 18. Upon increasing the heat current in small steps while in state (*b*), a power level would eventually be reached at which state (*b*) became unstable in the sense that it had a finite lifetime and eventually underwent a spontaneous transition to the state of lower heat transport (*c*). Prior to this transition, it was possible to measure the convective heat transport in the unstable state provided that its lifetime was not too short. Since the heat current was fixed in this experiment, the transition from (*b*) to (*c*) was accompanied by an increase in the Rayleigh number. While in state (*c*), decreasing the heat current in small steps would eventually result in a spontaneous transition to the high-conductivity state (*b*).

In figure 18, we have shown all points that were observed to be unstable as squares. There is of course no guarantee that the points shown as circles, for which no

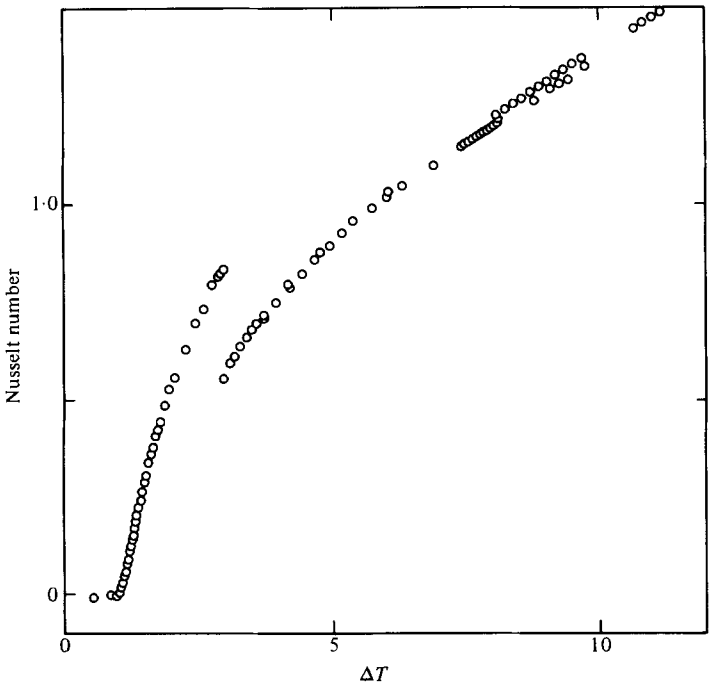

FIGURE 17. Nusselt numbers over a wide range of Rayleigh numbers for cell B. The results are shown as a function of the measured parameter ΔT, which is related to R/R_c by (6.12).

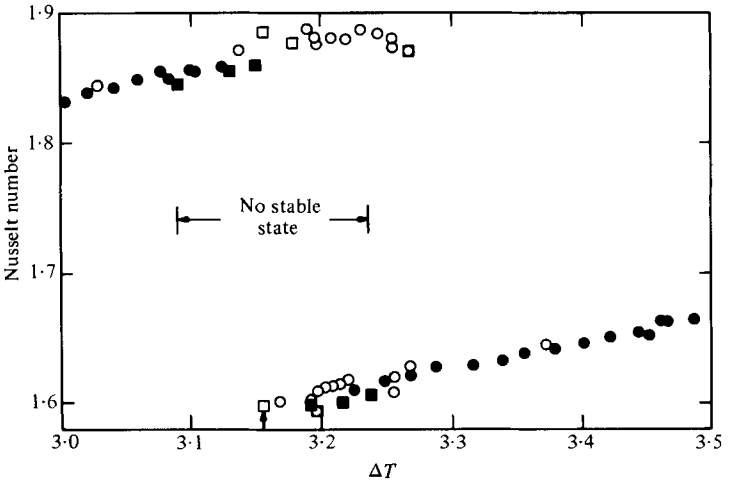

FIGURE 18. Nusselt numbers as a function of ΔT for cell B near the first discontinuous transition. Solid symbols are measurements at constant heat current; open symbols are measurements at constant ΔT. ■, □, unstable states for which transitions were observed; ●, ○, states for which no transition was observed during the duration of the experiment.

transition was observed, correspond to stable states. Many of them presumably would have undergone a transition if sufficient time had been allowed (most of the points were taken by waiting 30 minutes at a given heat current). We have indicated the range over which instability was observed either for state (*b*) or (*c*) in the figure, and presume that *all* measurements in that range would have yielded the instability if sufficient time had been allowed. For the same reasons, it is of course likely that the range of instability is in fact wider than indicated in the figure.

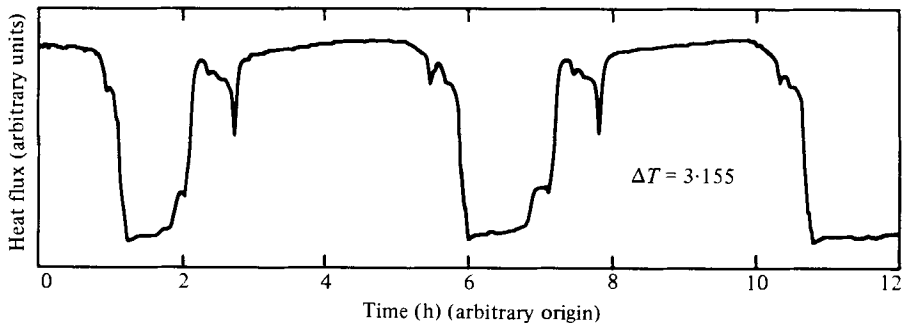

FIGURE 19. Time-dependent state for cell B at $\Delta T = 3{\cdot}155$ (see arrow near abscissa of figure 18). ΔT was fixed, and the time dependence is thus in the heat flux.

It can be seen that the data at constant heat current (solid symbols) for the unstable states in figure 18 leave a small region between $\Delta T = 3{\cdot}15$ and $3{\cdot}19$ in which it was not possible to maintain either state (*b*) or (*c*) sufficiently long to make a measurement. We therefore used the alternative method of holding constant the temperature difference across the cell and measuring the heat current required to do so. This procedure resulted in the open symbols in figure 18. It extended somewhat the range over which measurements could be made on the two branches. This procedure also revealed the instability of the two branches. However, at constant temperature difference a transition would require following a vertical path in figure 18. It is clear that the transition then is from one unstable state to another unstable state, provided that the Rayleigh number is in the range indicated in the figure. The result is that the convective heat transport becomes time-dependent. A sample of the time-dependence observed at $\Delta T = 3{\cdot}155$ is shown in figure 19. We note that the switching between the two states occurs on a very slow timescale. The regularity in the pattern suggests that the process is deterministic in character. The extremes in heat transport are plotted in figure 18 and identified by a small arrow near the abscissa. They correspond closely to the heat transport of states (*b*) and (*c*).

It is interesting to note that the occurrence of time-dependent states *at constant imposed heat current* has been predicted by Busse (1967*b*) for certain inverted bifurcations that yield a heat transport that has a gap as a function of Rayleigh number. The present case is different in that it occurs at constant imposed temperature difference.

Finally, we note that most of the scatter in figure 18 is not the result of limited experimental resolution, but is rather attributable to small deviations of the unstable system from a unique state.

Upon increasing ΔT beyond 3, the system remains in state (*c*) for $\Delta T \lesssim 10$. However, near $\Delta T = 9$, this state becomes periodically time-dependent. For $\Delta T > 10$, state (*c*) becomes unstable, and a new state (*d*) with a slightly larger convective heat transport evolves. Upon decreasing ΔT for state (*d*), a sizable hysteresis loop is observed extending down to $\Delta T \approx 8$. Upon decreasing ΔT and near $\Delta T = 8$, $N(\Delta T)$ for state (*d*) seems to merge continuously with $N(\Delta T)$ for state (*c*). State (*d*) also exhibits time dependence over a range of Rayleigh numbers. That time dependence has been discussed by Ahlers & Behringer (1978*a*, *b*) and by Ahlers (1980*b*).

7.5. *Uniqueness of* $N(R)$

Throughout the work on all three cells, we have searched for hysteresis and non-uniqueness of the states above R_c. In addition to the measurements described

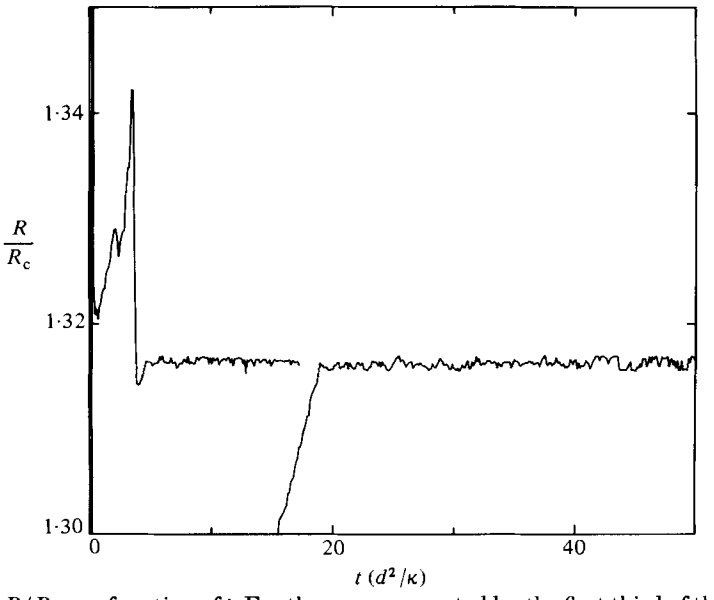

FIGURE 20. R/R_c as a function of t. For the run represented by the first third of the figure, a constant heat current q_1 was turned on discontinuously at $t = 0$. For the run represented by the rightmost two-thirds of the figure, a slow ramp in q was used to reach the same q_1. Both experiments yield final states with experimentally indistinguishable convective heat transport.

in detail above, we have usually made measurements using successive small steps in q. Invariably, we found within our resolution (of 0·001 or smaller) the same values of $N(R)$, regardless of whether q was increased or decreased. The only exceptions are of course the two hysteretic transitions for $L = 2{\cdot}08$, which were described in §7.4.

For cell A, we unsuccessfully attempted to induce different flow states by using different histories for the heat current prior to the steady-state heating period. An example is illustrated in figure 20. For the data in the left third of the figure, q was changed discontinuously from zero to some finite value $q_1 > 1$ at $t = 0$. The initial fast transients associated with pure thermal conduction have died out for $t \gtrsim O(1)$, and the onset of fluid flow decreases R/R_c from about 1·36 to about 1·32 rather rapidly. Thereafter, until $t \approx 5$, the system passes through various flow states, as indicated by the time dependence of R/R_c; but for $t > 5$ it settles down in a time-independent state, and any noise evident in figure 20 is of instrumental origin. Similar experiments, but with q *decreased* discontinuously from a value larger than q_1, yielded the same R/R_c in the steady state within experimental resolution. A third history for q is illustrated in the right two-thirds of figure 20. Here, the system was equilibrated at $q_0 < 1$, and then a very slow ramp in q was used to reach $q_1 > 1$. The ramp rate dq/dt was about 10^{-2}. At the end of the ramp, R/R_c immediately attains a steady-state value, and that value is equal to the steady-state value obtained with the step in q within the experimental resolution of 3×10^{-4} in R/R_c, corresponding to about 0·1 % of the *convective* heat transport $(N-1)\,R/R_c$. Thus we consider it very likely that the final states have the same spatial structure, regardless of history. In this respect, our cylindrical system is different from rectangular convection chambers, which seem to permit multistability with states corresponding to different numbers of convecting rolls. Our results are in this respect consistent, however, with those of Koschmieder & Pallas (1974) for cylindrical cells.

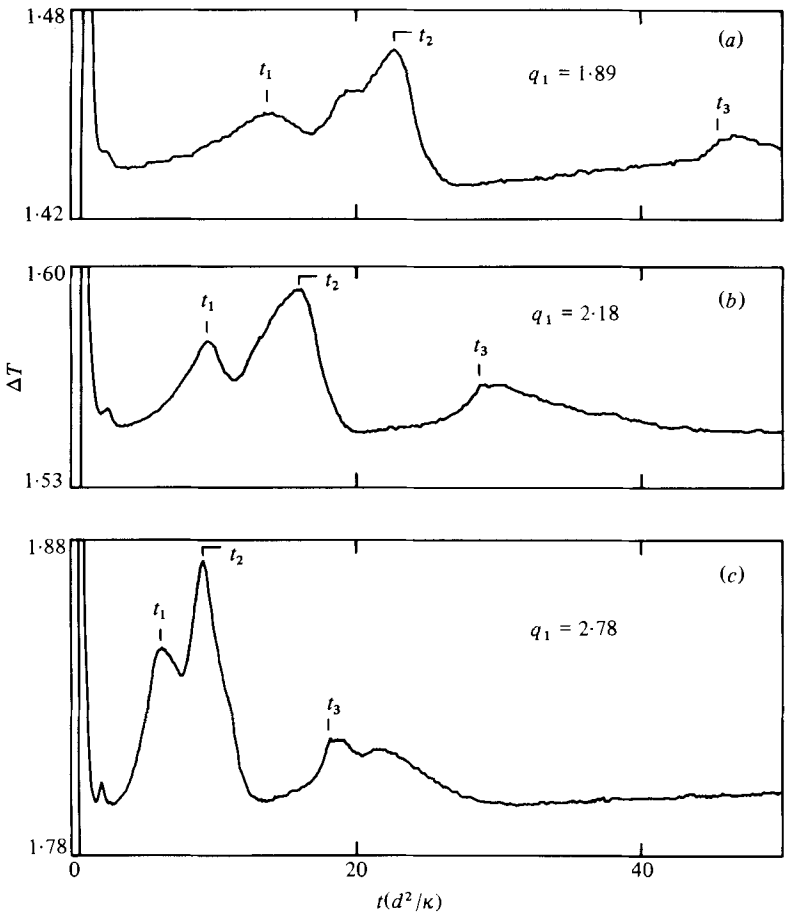

FIGURE 21. The dimensionless temperature difference ΔT as a function of t after a heat current q_1 is turned on at $t = 0$. Note the general similarity in the patterns, but also the change in timescale as q_1 is varied. The points identified as t_1, t_2 and t_3 are readily distinguishable features of the time evolution, and are used in figure 22.

7.6. *Transient effects*

From the results for cell A shown in figure 20, it can be seen that a step in q from $q_0 < 1$ to $q_1 > 1$ induces long-lived, transient, unstable convective states if q_1 is sufficiently large. We studied the evolution of the convective heat transport in detail as a function of q_1. In each case the step in q was from an initial value $q_0 = 0$. Results for ΔT (related to R/R_c by (6.12)) at several values of q_1 are shown in figure 21 for $t \leqslant 50$. The origin of the timescale of this figure coincides with the step in q. Repeated measurements with the same q_1 produced identical results within the experimental resolution. There is a steep maximum (off-scale in the figure) near $t = 1$ that is due to the fast transients involved in approaching a steady-state conducting temperature profile and the subsequent onset of convection (see also Behringer & Ahlers 1977, figure 2). For larger t, the temperature difference ΔT (and thus at constant q_1 also the convective heat transport $q_1 - \Delta T$) evolves in a complicated manner. There are several maxima, and we have identified the time of occurrence of three easily recognizable features near maxima as t_1, t_2 and t_3. As q_1 is increased, the overall shape of the curves in figure 21 remains largely unaltered; but the timescale of the evolution

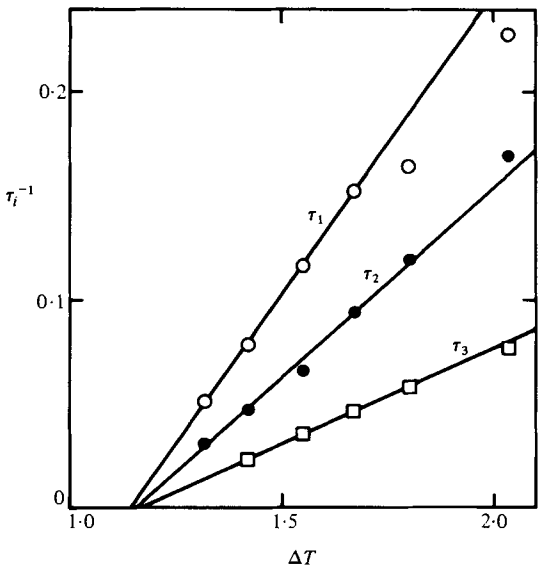

FIGURE 22. The inverse of $\tau_i = t_i - t_0$ (see figure 21), where $t_0 \approx 1$ is explained in the text. Note that all three sets of data cross the ΔT-axis near 1·16, suggesting that the initially excited mode has a convective onset that is higher than that of the final state.

becomes shorter. For the origin of that timescale, we chose the location t_0 of the initial large maximum near $t = 1$, and evaluated $\tau_i = t_i - t_0$. Figure 22 shows a plot of the experimental values of τ_1^{-1}, τ_2^{-1} and τ_3^{-1}. The data indicate that

$$\tau_i = \tau_0 \tilde{\epsilon}^{-1},$$

where

$$\tilde{\epsilon} \approx \bar{\epsilon} - 0{\cdot}16.$$

Thus the unstable, transient state exhibits the type of slowing down that is well known for normal bifurcations; but the value of the critical Rayleigh number for this state is larger than R_c by about 16%.

The transient behaviour is shown over an even larger time interval in figure 23. For each q_1, we show two separate experimental runs to demonstrate the extent to which the measurements are reproducible. The early parts of these runs have similar features, which evolve more quickly at larger q_1 (as shown in figure 21). But the later parts of the runs show that a 'steady state' is reached sooner at the smaller q_1. As q_1 increases, the time evolution of ΔT becomes more complicated, and therefore lasts longer, even though a given feature evolves earlier. At the highest q_1 shown (runs (*g*) and (*h*)), the fluid flow in the longtime limit is non-periodically time-dependent (Ahlers 1974, 1980*b*; Ahlers & Behringer 1978*a*, *b*; Behringer *et al.* 1982), and thus the initial evolution of ΔT becomes non-reproducible after a relatively short time.†

The results of five nominally identical runs of even longer duration and with $q_1 = 2{\cdot}93$ have been shown by Ahlers & Walden (1980, figure 4). Those measurements showed that the reproducibility that is demonstrated in figure 22 extends at that q_1 to times as large as $300t_v$. Eventually, however, the time evolution of nominally identical runs ceases to be the same. We believe that this 'getting lost' is associated

† Even at the smaller values of q_1, the flow is non-periodic at large time (Walden & Ahlers 1981); but the timescale of that non-periodic behaviour is so long that it is not perceptible on the scale of figures 21 and 23.

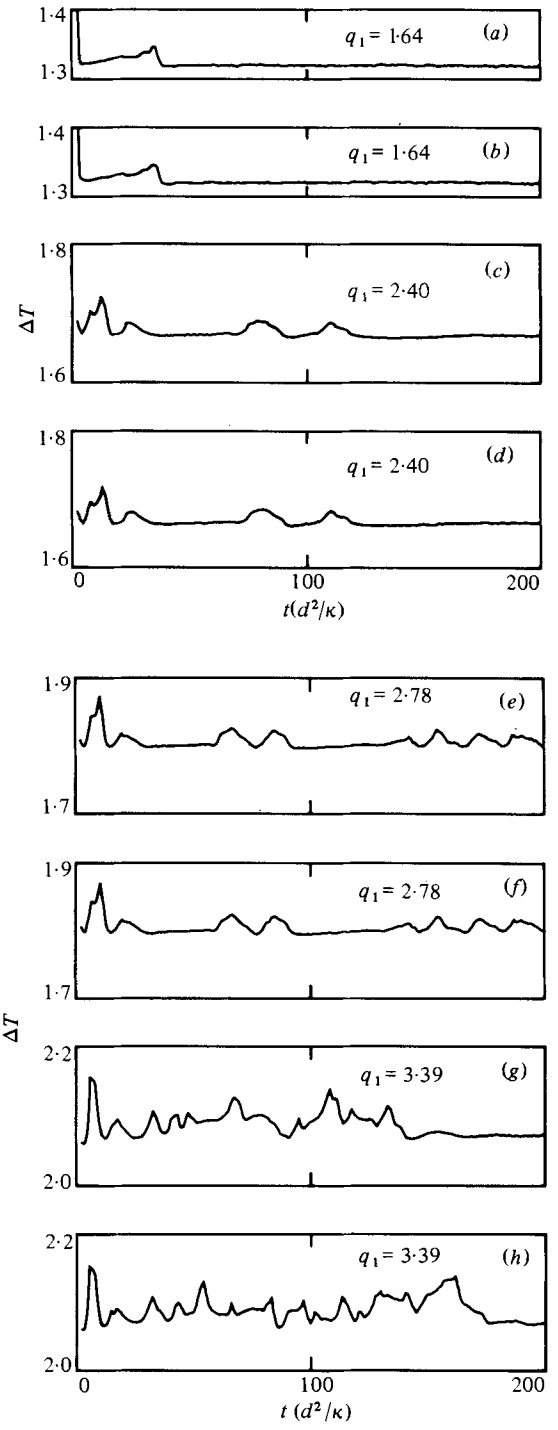

FIGURE 23. The dimensionless temperature difference ΔT as a function of t after a heat current q_1 is turned on at $t = 0$. These data are over a longer time interval than those of figure 21. For each q_1, two separate experimental runs are shown to demonstrate the extent of the reproducibility of even quite complicated evolutions (e and f). At sufficiently high q_1, corresponding to $\Delta T \gtrsim 2$, the evolution is no longer reproducible because the system is clearly turbulent on the time-scale of these experiments. See also figure 4 of Ahlers & Walden (1980).

with the intrinsic time dependence of the flow that exists at the Rayleigh numbers corresponding to that q_1 (Ahlers & Walden 1980). The data of Ahlers & Walden also show that the early evolution, although often reproducible, need not be the same in every nominally identical experiment. Instead, for five runs, they discovered two distinct time histories. Thus it appears that for a given set of nominally identical initial conditions there exists a small number of discrete paths to the long-time behaviour of the system.

8. Summary

In the first part of this paper, we presented a detailed description of our apparatus and of procedures for the investigation of heat transport in shallow horizontal layers of fluid at low temperatures. The results of several experiments conducted with this apparatus have already been reported elsewhere. These include the investigations of non-Boussinesq effects on Rayleigh–Bénard convection (Walden & Ahlers 1981), of the transients involved in the evolution of fluid flow close to the onset of convection (Ahlers *et al.* 1981) and of time-dependent states in convecting fluid layers of several different aspect ratios (Ahlers & Behringer 1978*a*, *b*; Ahlers 1980*b*; Ahlers & Walden 1980; Greenside *et al.* 1982). A brief summary of much of this work is given by Ahlers (1980*b*).

In the second half of this paper, we presented additional results that pertain primarily to the behaviour of Boussinesq fluid layers of aspect ratio $L = 2{\cdot}08$, $4{\cdot}72$ and 57 in the long-time limit. In addition, we discuss our observations of complicated, long-lived, reproducible transients that occur when the fluid layer with $L = 4{\cdot}72$ is heated impulsively to a Rayleigh number well above the convective onset. Our results are as follows.

For $L = 2{\cdot}08$ and $4{\cdot}72$, critical Rayleigh numbers R_c were determined with high precision, but possible systematic errors are as large as 15%. The ratio of R_c for the two cells is subject to much smaller systematic errors, and is found to be $R_c^{2{\cdot}08}/R_c^{4{\cdot}72} = 1{\cdot}06 \pm 0{\cdot}02$. This result is compared with the calculations by Charlson & Sani (1970, 1971), the predictions based on the amplitude equation (Ahlers *et al.* 1981) and the measurements by Stork & Müller (1975). It is consistent both with a flow pattern of straight rolls and with a cylindrically symmetric pattern with finite centre amplitude. It tends to rule out a pattern of cylindrical symmetry and vanishing centre amplitude, such as the one considered by Ahlers *et al.* (1981).

Very detailed measurements of Nusselt numbers $N(R)$ near R_c were made in order to study the sharpness of the convective onset. For $L = 2{\cdot}08$ and $4{\cdot}72$, any rounding of the transition is only slightly larger than the experimental resolution, and $N(R_c) - 1 \approx 10^{-3}$. An earlier investigation in a cell with $L = 5{\cdot}27$ and with horizontal plates not nearly close to being parallel as those of the present cells (Ahlers 1974, 1975) had yielded $N(R_c) - 1 \approx 0{\cdot}03$. The present results show that the onset of convective flow can be essentially sharp even in containers of finite lateral extent. The bifurcation becomes imperfect, however, when the cell spacing in non-uniform. These results agree with the theoretical work of Reiss (1977), Kelly & Pal (1978) and Tavantzis *et al.* (1978). From theory, it is expected also that the bifurcation should become imperfect if the lateral boundaries are 'imperfectly insulating' and there is lateral heat flow into the sidewalls even in the absence of convection (Daniels 1977; Hall & Walton 1977; Brown & Stewartson 1978). Since we see almost no rounding for $L = 4{\cdot}72$ and $2{\cdot}08$, we conclude that our sidewalls are not imperfectly insulating. These results indicate that our attempts to attach the sidewalls thermally to the top

and bottom plates (see §2.3.1) were successful. For the large-aspect-ratio cell ($L = 57$), the rounding of $N(R)$ near R_c was much more severe, and $N(R_c) - 1 \approx 0{\cdot}03$. This cell had a much smaller height than the others, and the same variation of the spacing between the top and bottom plates corresponds to a greater relative variation of the layer thickness, thus explaining the greater rounding.

The Nusselt numbers $N(R)$ above but close to R_c were measured in detail for each cell, and the initial slopes $N_1 = dN/d(R/R_c)$ just above R_c were determined. For $L = 2{\cdot}08$ and $4{\cdot}72$, an unstable state is created first, even when R_c is exceeded very slowly. At large time, this state decays to another convecting state; but it is sufficiently long-lived that its initial slope N_1 could be measured. For $L = 2{\cdot}08$, we found $N_1 = 0{\cdot}36$, in excellent agreement with calculations by Charlson & Sani (1975) for similar values of L, insulating sidewalls, and for a state with cylindrical symmetry and finite centre amplitude. An unstable state of cylindrical symmetry has been observed also by Kirchartz *et al.* (1981) for $L \approx 3$ when in their experiment the convecting state was entered fairly rapidly from below R_c. For $L = 4{\cdot}72$, we found $N_1 = 0{\cdot}56$ for the unstable state. No calculations are available for this aspect ratio. Numerical studies similar to those for smaller L (Charlson & Sani 1975) would be most interesting for comparison. For the two cells with $L = 2{\cdot}08$ and $4{\cdot}72$, the relative values of R_c, the initial slopes of N and the instability of the initially formed state, when compared with theory and the experiments of Kirchartz *et al.*, thus strongly support the idea that the fluid flow initially has cylindrical symmetry with finite amplitude at the centre. Since this state decays at later times, the stable state is presumably not of cylindrical symmetry. For $L = 57$, we found $N_1 = 1{\cdot}25$. This value is only about 12 % less than the theoretical value $N_1 = 1{\cdot}431$ for a laterally infinite system of straight rolls (Schlüter *et al.* 1965). Since our convecting fluid in this cell showed time-dependent behaviour, the pattern almost surely contained many defects and deviations from straight-roll flow, and we assume that these irregularities account for the slight difference between the theoretical and experimental values of N_1.

For all three cells, Nusselt numbers were measured also at larger R. For $L = 57$ and $R \lesssim 2{\cdot}3R_c$, and for $L = 4{\cdot}72$ and $R \lesssim 24\,R_c$, $N(R)$ was (within our resolution) a unique, smoothly varying and monotonically increasing function of R. For $L = 2{\cdot}08$, however, $N(R)$ revealed two discontinuous transitions with hysteresis, one near $3R_c$ and one near $10R_c$. We assume that these transitions correspond to changes in the symmetry of the flow pattern.

Particularly for $L = 4{\cdot}72$, we searched for non-uniqueness of the state above R_c by varying the thermal history of the sample. By heating impulsively on the one hand, and by entering the convecting state with a slow ramp on the other, we obtained convective heat transport $(N-1)R/R_c$ near $1{\cdot}3R_c$ that was the same within one part in 10^3. Thus we were unable to induce measurably different states above R_c for this cell.

Finally, the last result reported in this paper is the existence of long-lived, complicated, but reproducible, transients that evolve for $L = 4{\cdot}72$ when the heat current is turned on suddenly. Reproducible, complicated behaviour has been observed for times as long as 300 vertical thermal diffusion times.

The experiments described in this paper were done while the authors were at Bell Laboratories, Murray Hill, NJ 07974. We are grateful to M. C. Cross and P. C. Hohenberg for informative discussions. The work of G. A. was supported in part by NSF grant DMR79-23289.

REFERENCES

AHLERS, G. 1971*a* Heat capacity near the superfluid transition in ^{4}He at saturated vapor pressure. *Phys. Rev.* A **3**, 696–716.

AHLERS, G. 1971*b* On the viscosity of ^{4}He near the superfluid transition. *Phys. Lett.* **37** A, 151–152.

AHLERS, G. 1974 Low temperature studies of the Rayleigh–Bénard instability and turbulence. *Phys. Rev. Lett.* **33**, 1185–1188.

AHLERS, G. 1975 The Rayleigh–Bénard instability at helium temperatures. In *Fluctuations, Instabilities and Phase Transitions* (ed. T. Riste), pp. 181–193. Plenum.

AHLERS, G. 1976 Experiments near the superfluid transition in ^{4}He and ^{3}He–^{4}He mixtures. In *The Physics of Liquid Helium*, Part I (ed. K. H. Bennemann & J. B. Ketterson), pp. 85–206. Wiley.

AHLERS, G. 1978 Thermal conductivity of ^{4}He vapor as a function of density. *J. Low Temp. Phys.* **31**, 429–439.

AHLERS, G. 1980*a* Effect of departures from the Oberbeck–Boussinesq approximation on the heat transport of horizontal convecting fluid layers. *J. Fluid Mech.* **98**, 137–148.

AHLERS, G. 1980*b* Onset of convection and turbulence in a cylindrical container. In *Systems far from Equilibrium* (ed. L. Garrido), pp. 143–161. Springer.

AHLERS, G. & BEHRINGER, R. P. 1978*a* The Rayleigh–Bénard instability and the evolution of turbulence. *Prog. Theor. Phys. Suppl.* **64**, 186–201.

AHLERS, G. & BEHRINGER, R. P. 1978*b* Evolution of turbulence from the Rayleigh–Bénard instability. *Phys. Rev. Lett.* **40**, 712–716.

AHLERS, G., CROSS, M. C., HOHENBERG, P. C. & SAFRAN, S. 1981 The amplitude equation near the convective threshold: applications to time-dependent heating experiments. *J. Fluid Mech.* **110**, 297–334.

AHLERS, G., HOHENBERG, P. C. & KORNBLIT, A. 1982 Nonlinear renormalization-group analysis of the thermal conductivity of ^{4}He for $T \geqslant T_\lambda$. *Phys. Rev.* B **25**, 3136–3166.

AHLERS, G. & WALDEN, R. W. 1980 Turbulence near onset of convection. *Phys. Rev. Lett.* **44**, 445–448.

BARENGHI, C. F., LUCAS, P. G. J. & DONNELLY, R. J. 1981 Cubic spline fits to thermodynamic and transport parameters of liquid ^{4}He above the λ transition. *J. Low Temp. Phys.* **44**, 491–503.

BECKER, E. W., MISENTA, R. & SCHMEISSNER, F. 1954*a* Die Zähigkeit von gasförmigem He^3 and He^4 zwischen 1,3 °K and 4,2 °K. *Z. Phys.* **137**, 126–136.

BECKER, E. W., MISENTA, R. & SCHMEISSNER, F. 1954*b* Viscosity of gaseous He^3 and He^4 between 1·3 °K and 4·2 °K. *Phys. Rev.* **93**, 244–245.

BECKER, E. W. & MISENTA, R. 1955 Die Zähigkeit von HD and He^3 zwischen 14 °K and 20 °K. *Z. Phys.* **140**, 535–539.

BEHRINGER, R. P., AGOSTA, C., JAN, J. S. & SCHAUMEYER, J. N. 1980 Time dependent Rayleigh–Bénard convection and instrumental attenuation. *Phys. Lett.* **80** A, 273–276.

BEHRINGER, R. P. & AHLERS, G. 1977 Heat transport and critical slowing down near the Rayleigh–Bénard instability in cylindrical containers. *Phys. Lett.* **62** A, 329–331.

BEHRINGER, R. P., SHAUMEYER, J. N., JAN, J. S., CLARK, C. A. & AGOSTA, C. 1982 Turbulent onset in moderately large aspect ratios. *Phys. Rev.* A (in press).

BÉNARD, H. 1900 Les tourbillons cellulaires dans une nappe liquide. *Rev. Gen. Sci. Pure Appl.* **11**, 1261–1271, 1309–1328.

BÉNARD, H. 1901 Les tourbillons cellulaires dans une nappe liquide transportant de la chaleur par convection en régime permanent. *Ann. Chim. Phys.* **23**, 62–144.

BOUSSINESQ, J. 1903 *Théorie Analytique de la Chaleur*, vol. 2. Gauthier-Villas.

BROWN, S. N. & STEWARTSON, K. 1978 On finite amplitude Bénard convection in a cylindrical container. *Proc. R. Soc. Lond.* A **360**, 455–469.

BUSSE, F. H. 1967*a* The stability of finite amplitude cellular convection and its relation to an extremum principle. *J. Fluid Mech.* **30**, 625–649.

BUSSE, F. H. 1967*b* Non-stationary finite amplitude convection. *J. Fluid Mech.* **28**, 223–239.

CHANDRASEKHAR, S. 1961 *Hydrodynamic and Hydromagnetic Stability*. Clarendon.

CHARLSON, G. S. & SANI, R. L. 1970 Thermoconvective instability in a bounded cylindrical fluid layer. *Int. J. Heat Mass Transfer* **13**, 1479–1496.

CHARLSON, G. S. & SANI, R. L. 1971 On thermoconvective instability in a bounded cylindrical fluid layer. *Int. J. Heat Mass Transfer* **14**, 2157–2160.

CHARLSON, G. S. & SANI, R. L. 1975 Finite amplitude axisymmetric thermoconvective flows in a bounded cylindrical layer of fluid. *J. Fluid Mech.* **71**, 209–229.

CROSS, M. C., DANIELS, P. G., HOHENBERG, P. C. & SIGGIA, E. D. 1980 Effect of sidewalls in wavenumber selection in Rayleigh–Bénard convection. *Phys. Rev. Lett.* **45**, 898–901.

CROSS, M. C., DANIELS, P. G., HOHENBERG, P. C. & SIGGIA, E. D. 1983 Phase-winding solutions in a finite container above the convective threshold. *J. Fluid Mech.* (in press).

DANIELS, P. G. 1977 The effect of distant sidewalls on the transition to finite amplitude Bénard convection. *Proc. R. Soc. Lond.* A **358**, 173–197.

DELONG, L. E., SYMKO, O. G. & WHEATLEY, J. G. 1971 Continuously operating ^{4}He evaporation refrigerator. *Rev. Sci. Instrum.* **42**, 147–150.

DIJK, H. VAN, DURIEUX, M., CLEMENT, J. R. & LOGAN, J. K. 1960 The '1958 ^{4}He Scale of Temperatures'. *Nat. Bur. Standards Monograph* no. 10.

GOODWIN, J. 1968 The pressure dependence of viscosity in liquid helium. Ph.D. thesis, University of Washington.

GREENSIDE, H. S., AHLERS, G., HOHENBERG, P. C. & WALDEN, R. W. 1982 A simple stochastic model for the onset of turbulence in Rayleigh–Bénard convection. *Physica* D (to be published).

HALL, P. & WALTON, I. C. 1977 The smooth transition to a convective regime in a two-dimensional box. *Proc. R. Soc. Lond.* A **358**, 199–221.

HIRSCHFELDER, J. O., CURTISS, C. F. & BIRD, R. B. 1967 *Molecular Theory of Gases and Liquids*, chap. 8.2. Wiley.

KELLER, W. E. 1969 *Helium-3 and Helium-4*, p. 86. Plenum.

KELLY, R. E. & PAL, D. 1978 Thermal convection with spatially periodic boundary conditions: resonant wavelength excitation. *J. Fluid Mech.* **86**, 433–456.

KIRCHARTZ, K. R., MÜLLER, U., OERTEL, H. & ZIEREP, J. 1981 Axisymmetric and non-axisymmetric convection in a cylindrical container. *Acta Mechanica* **40**, 181–194.

KOSCHMIEDER, E. L. 1974 Bénard convection. *Adv. Chem. Phys.* **26**, 177–212.

KOSCHMIEDER, E. L. & PALLAS, S. G. 1974 Heat transfer through a shallow horizontal convecting fluid layer. *Int. J. Heat Mass Transfer* **17**, 991–1002.

KRISHNAMURTI, R. 1968 Finite amplitude convection with changing mean temperature. Part 2. An experimental test of the theory. *J. Fluid Mech.* **33**, 457–463.

KRISHNAMURTI, R. 1970*a* On the transition to turbulent convection. Part 1. The transition from two- to three-dimensional flow. *J. Fluid Mech.* **42**, 295–307.

KRISHNAMURTI, R. 1970*b* On the transition to turbulent convection. Part 2. The transition to time-dependent flow. *J. Fluid Mech.* **42**, 309–320.

KRISHNAMURTI, R. 1973 Some further studies on the transition to turbulent convection. *J. Fluid Mech.* **60**, 285–303.

LEE, G., LUCAS, P. & TYLER, A. 1979 Bénard instability measurements in ^{3}He–^{4}He mixtures near their lambda temperatures. *Phys. Lett.* **75**A, 81.

LIBCHABER, A. & MAURER, J. 1978 Local probe in a Rayleigh–Bénard experiment in liquid helium. *J. Physique Lett.* **39**, L369–L372.

LIBCHABER, A. & MAURER, J. 1980 Une expérience de Rayleigh–Bénard de géometrie reduite: multiplication, accrochage et démultiplication de fréquences. *J. Physique Coll.* C **3**, 41–51.

LIBCHABER, A. & MAURER, J. 1981 A Rayleigh–Bénard experiment: helium in a small box. *Proc. NATO Conf., Geilo, Norway.* To be published.

MALKUS, W. V. R. 1954 Discrete transitions in turbulent convection. *Proc. R. Soc. Lond.* A **225**, 185–195.

MAURER, J. & LIBCHABER, A. 1979 Rayleigh–Bénard experiment in liquid helium: frequency locking and the onset of turbulence. *J. Physique Lett.* **40**, 419.

MAURER, J. & LIBCHABER, A. 1980 Effect of the Prandtl number on the onset of turbulence in liquid ^{4}He. *J. Physique Lett.* **41**, 515.

MUELLER, K. H., AHLERS, G. & POBELL, F. 1976 Thermal expansion coefficient, scaling, and universality near the superfluid transition of ^{4}He. *Phys. Rev.* B **14**, 2096–2118.

NIELD, D. A. 1968 The Rayleigh–Jeffreys problem with boundary slab of finite conductivity. *J. Fluid Mech.* **32**, 393–398.

OBERBECK, A. 1879 Über die Wärmeleitung der Flüssigkeiten bei der Berücksichtigung der Strömungen infolge von Temperatur-Differenzen. *Ann. Phys. Chem.* **7**, 271–292.

PALLAS, S. G. 1972 Heat transfer and wavelength measurement for axisymmetric flow of a fluid heated from below. Ph.D. thesis, University of Texas.

RAYLEIGH, LORD 1916 *Phil. Mag.* **32**, 529–546.

REISS, E. L. 1977 Imperfect bifurcation. In *Application of Bifurcation Theory*, pp. 37–71. Academic.

ROSSBY, H. T. 1969 A study of Bénard convection with and without rotation. *J. Fluid Mech.* **36**, 309–335.

SCHLÜTER, A., LORTZ, D. & BUSSE, F. 1965 On the stability of steady finite amplitude convection. *J. Fluid Mech.* **23**, 129–144.

SCHMIDT, R. J. & MILVERTON, S. W. 1935 On the instability of a fluid when heated from below. *Proc. R. Soc. Lond.* A **152**, 586–594.

SCHMIDT, R. J. & SAUNDERS, O. A. 1938 On the motion of a fluid heated from below. *Proc. R. Soc. Lond.* A **165**, 216–228.

SILVESTON, P. L. 1958 Wärmedurchgang in waagerechten Flüssigkeitsschichten. *Forsch. Ing. Wes.* **24**, 29–32, 59–69.

SPARROW, E. M., GOLDSTEIN, R. J. & JONSSON, V. R. 1964 Thermal instability in a horizontal fluid layer: effect of boundary conditions and non-linear temperature profile. *J. Fluid Mech.* **18**, 513–528.

STEINBERG, V. 1980 Undamped second sound waves in the He^3–He^4 mixture heated from below. *Phys. Rev. Lett.* **45**, 2050–2052.

STEINBERG, V. 1981*a* Stationary convective instability in a superfluid He^3–He^4 mixture. I. *Phys. Rev.* A **24**, 975–987.

STEINBERG, V. 1981*b* Oscillatory convection instability in a superfluid He^3–He^4 mixture. II. *Phys. Rev.* A **24**, 2584–2594.

STORK, K. & MÜLLER, U. 1975 Convection in boxes: an experimental investigation in vertical cylinders and annuli. *J. Fluid Mech.* **71**, 231–240.

STRATY, G. C. & ADAMS, E. D. 1969 Highly sensitive capacitive pressure gauge. *Rev. Sci. Instrum.* **40**, 1393–1397.

TAVANTZIS, J., REISS, E. L. & MATKOWSKY, B. 1978 On the smooth transition to convection. *SIAM J. Appl. Math.* **34**, 322–337.

THRELFALL, D. C. 1975 Free convection in low-temperature gaseous helium. *J. Fluid Mech.* **67**, 17–28.

TJERKSTRA, H. H. 1952 The influence of pressure on the viscosity of liquid helium. I. *Physica* **18**, 853–861.

VAN DEGRIFT, C. T. 1974 Dielectric constant, density, and expansion coefficient of liquid ^{4}He at vapor pressure below 4·4 K. Ph.D. thesis, University of California, Irvine.

VAN ITTERBEEK, A., SCHAPINK, F. W., VAN DEN BERG, G. J. & VAN BEEK, H. J. M. 1953 Measurements of the viscosity of He-gas at liquid helium temperatures as a function of temperature and pressure. *Physica* **19**, 1158–1162.

WALDEN, R. W. & AHLERS, G. 1981 Non-Boussinesq and penetrative convection in a cylindrical cell. *J. Fluid Mech.* **109**, 89–114.

WARKENTIN, P. A., HAUCKE, H. J. & WHEATLEY, J. C. 1980 Convection in dilute solutions of ^{3}He in superfluid ^{4}He. *Phys. Rev. Lett.* **45**, 918–921.

WILLIS, G. E. & DEARDORFF, J. W. 1967 Confirmation and renumbering of the discrete heat flux transitions of Malkus. *Phys. Fluids* **10**, 1861–1866.

WILLIS, G. E., DEARDORFF, J. W. & SOMERVILLE, R. C. J. 1972 Roll-diameter dependence in Rayleigh convection and its effect upon the heat flux. *J. Fluid Mech.* **54**, 351–367.

WONSIEWICZ, B. D., STORM, A. R. & SIEBER, J. D. 1978 Microcomputer control of apparatus, machinery, and experiments. *Bell Syst. Tech. J.* **57**, 2209–2232.